CHAPTER 4 NUMERICAL MODELING OF A LATE MIXING POROUS BURNER (LMPB) FOR GASEOUS FUEL

Most of the early studies were focused on the premixed flame stabilized within the porous inert media. However, the premixed flame does not popular in industrial applications as compared with the diffusion flame. Fuel and air have lots of time to meet and mix in a mixing section. This is results in a risk of auto-ignition outside the combustion chamber. Only a few researches have been focused on safety late mixing combustion within porous inert media.

This chapter concerns the development of a numerical modeling of late mixing porous burner (hereafter referred to as LMPB) for liquefied petroleum gas (LPG). The LMPB can be operated both in case of non-preheated and preheated air by adjusting an air jacket. The objectives of this study are to present the thermal structure and burner performance in term of radiant output efficiency of LMPB. The numerical modeling in case of non-preheated air was developed at first; after that the modified numerical modeling in case of preheated air was performed. The numerical results are compared with available experimental data in order to validate model accuracy. Subsequently, parametric studies, i.e., equivalence ratio, firing rate, air preheating, and porous type are accomplished to investigate the burner performance. Moreover, the comparison between in case of non-preheated air and preheated air is presented. In the last topic of this chapter, the summary results are presented.

4.1 Numerical model

4.1.1 Burner geometry

Figure 4.1 and 4.2 show a schematic diagram of a one dimensional model for the late mixing porous burner (LMPB) in case of non-preheated and with preheated air respectively. The fuel and air supplies are separated for safety reason. The LMPB is divided into three sections: the fuel-preheated porous medium (FP), the porous

combustor (PC) and the mixing chamber, which is small space between FP and PC. The FP is made of metallic wire screen with mesh size of 100 mesh/in, whereas the PC is composed of a packed bed of inert solid spheres with diameter of 10 mm. The total length of the burner is 260 mm (FP section is 80 mm long, mixing chamber is 20 mm long and PC section is 160 mm long).The computation domain is discretized into 200 grid points (100 grid points in FP and 100 grid points in PC). Both ends of the system are exposed to black surfaces maintained at ambient temperature T_0 providing incident radiance $I_0^+\left(\tau_{-x_{FP}}\right)$ and $I_0^-\left(\tau_{PC}\right)$, respectively.

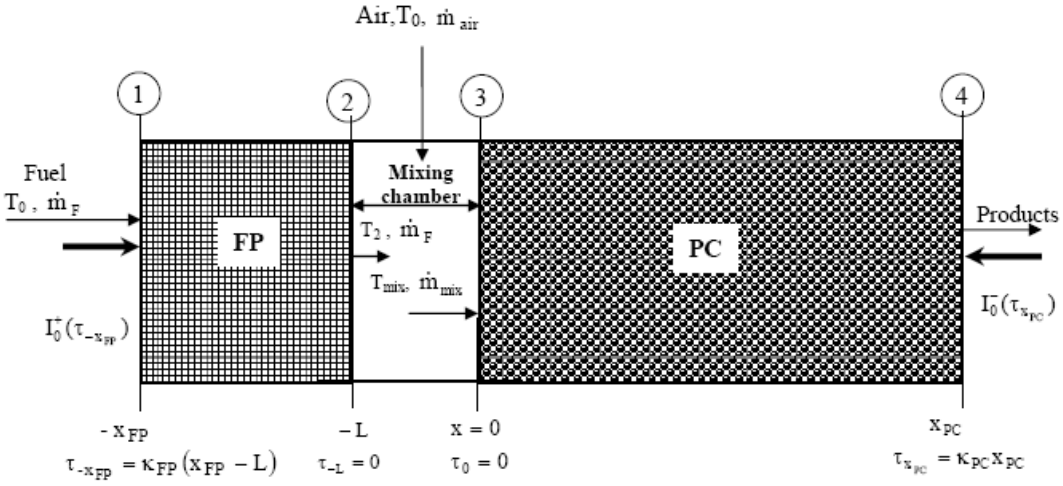

Figure 4.1 Burner geometry in case of non-preheated air.

In case of non-preheated air (show in Fig. 4.1), the fuel with initial temperature T_0 flows into the porous FP at section (1) ($x = -x_{FP}$) and heat is transferred from FP to the fuel. Then, the fuel with temperature at T_2 and the swirling air with temperature at T_0 meet and mix together in the mixing chamber in a short time with a late mixing fashion such that a homogeneous combustible mixture of fuel and air can be formed using a highly swirling flow motion of the combustion air. The mixture flows through PC at section (3) with a homogeneous temperature at T_{mix} prior to an immediate combustion within the PC. After that, the exhaust gas flow out the system at section (4).

Figure 4.2 show the burner geometry n case of preheated air. Different in case of non-preheated air, the PC is surrounded by an air jacket, which is used as an air preheating component. The gaseous fuel at T_0 flows into the FP at section (1) and is preheated by the hot porous matrix. At the same time, the combustion air with inlet temperature T_{ai} flows through an annular air jacket at section (4), and is preheated. The hot fuel and the hot air, which flow out from section (2) of FP and section (3) of the air jacket, respectively, meet and mix together in the mixing chamber. The homogeneous combustible mixture temperature at T_{mix} flow through the PC and is burned in this place.

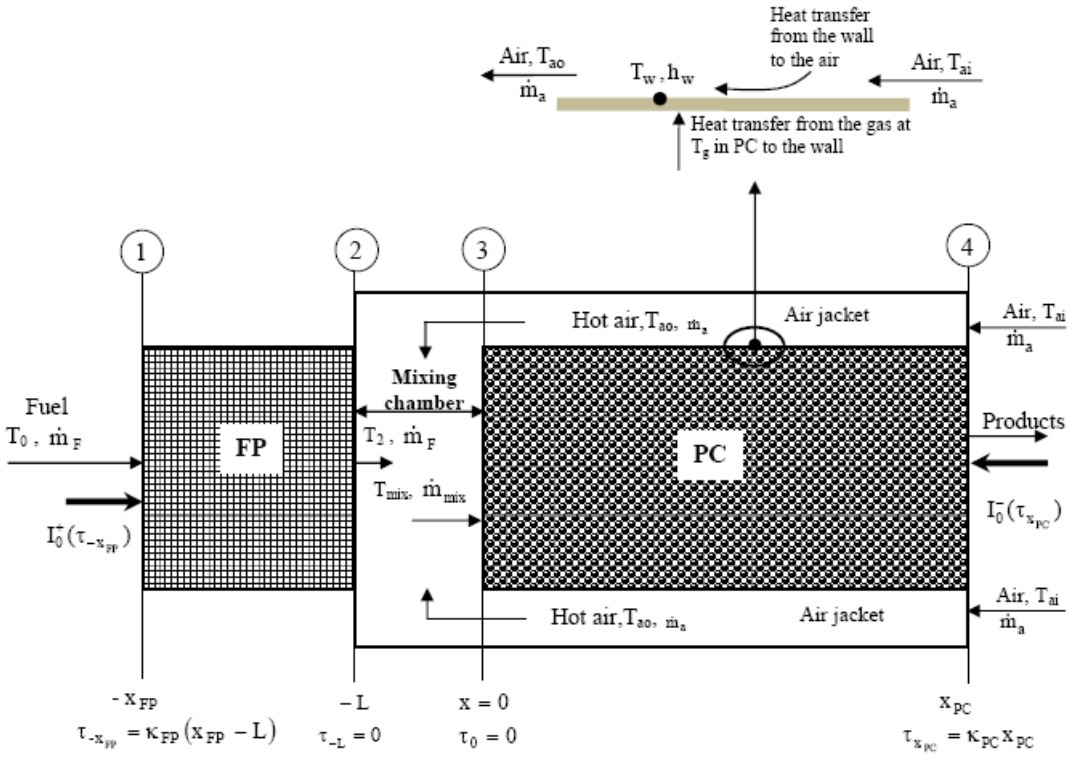

Figure 4.2 Burner geometry in case of preheated air.

The LMPB can yield a more safety in operation as compared with the conventional, premixed porous burner since the fuel and air are separately supplied through the LMPB before mixing. Therefore, a risk of undesirable auto-ignition can be avoided. The LMPB can allow for an efficient air preheating and thus resulting in an enhancement in its thermal performance and combustion characteristics. The effects of solid and gas phase conduction, solid radiation, and heat exchange between the solid and gas phases are also considered in the numerical model.

4.1.2 Principal assumptions

The principal assumptions are considered in the combustion model both in case of non-preheated air and preheated air are as follows:

(a) The system is good thermal insulation so no radial energy losses occur from cylindrical system, so that the solution can be obtained using one-dimensional for flow and heat transfer (Howell et al., 1996). Moreover, in combustion within porous media problems, the pore length scale is not the smallest length scale to be considered. The pore length scale is significantly larger than the thickness of the reaction zone. For this reason, the gas in the PC can be treated as a one-dimensional reactive flow and interaction between gas and solid is through heat exchange that is proportional to the temperature difference between the solid and gas (Henneke and Ellzey, 1999).

(b) Steady state and steady flow process.

(c) Non-radiating working gas behaves as ideal gases.

(d) FP and PC are able to emit and absorb thermal radiation in local thermal equilibrium, while radiative scattering is ignored.

(e) The flow is incompressible, because the flow velocity is very small when compared to the sound speed.

(f) The effect of pressure drop on the thermal structure is not significant (El-Hossaini et.al., 2008) and the measured pressure drop in this study is small so the effect of pressure drop is ignored.

(g) The Lewis number is unity.

(h) The physical properties are constant.

(i) Ends of porous media both in FP and PC are insulated the boundary condition at that ends will be that the derivative of temperature must be zero (Goodwine,

2010). At steady state condition, the two porous media are coupled by radiative heat transfer emitted from the PC to the FP for preheating the fuel. At the burner exit, the reaction has reached equilibrium, so that the gradient in product mole fraction equals to zero.

(j) Porous media are non-catalytic both in FP and PC.

(k) In FP, the mechanisms of hydrocarbon thermal cracking are negligible.

(l) The combustion reaction is described by an irreversible first-order reaction: Reactants$\rightarrow$ Products.

(m) The fuel/air mixture at temperature T_{mix} is completely premixed as it enters the PC at section (3).

(n) From experimental results, the peak temperature is located within PC. This implies that the main combustion was occurred in the PC. Thus, in this model considers that the reaction starts and gets completed only in PC. Flame location is not fixed but is varied depending on operating condition i.e. equivalence ratio and firing rate.

(o) The mixing chamber is assumed control volume under steady flow condition. The preheated fuel is mixed with the air at a specified temperature. The energy of the outgoing mixture is the total energies of the incoming streams of fuel and air. The mass flow rate of the outgoing mixture equal sum of the incoming mass flow rates so the flow velocity within the PC is higher than the flow velocity within the FP.

(p) In case of preheated air, the PC wall temperature at T_w is constant because of good thermal conductivity.

First the general forms of the equations in case of non-preheated air and preheated air are stated. Later section will present issues relating to solving the equations.

4.1.3 Basic equations in case of non-preheated air

In case of non-preheated air the computational domains consist of three main parts: In FP section, mixing chamber section and in the PC section. The numerical model is a one-dimensional reacting flow that interacts with the solid phase through a volumetric heat transfer coefficient. Single step first order reaction, solid and gas phase conduction, solid radiation are also included in the model. Gas phase radiation is insignificant and is excluded from the model due to the small optical path lengths involved, while thermal diffusivity in the gas phase is neglected because diffusion is considered to be negligible (Henneke, 1999). The model considers one-dimensional relations that the porous materials are the source of radiative emission and absorptions, but the gas within the pores can be treated as transparent; and the flow through two porous is incompressible and one-dimensional, so that the momentum equation need not be solved explicitly (Howell et al., 1996). The governing equations are as follows.

In the FP section, $-x_{FP} \le x \le -L \ \left(\tau_{-x_{FP}} \le \tau \le \tau_{-L}\right)$,

the conservation equations for energy of gas and solid phase are given by

$$\rho_F c_F \varepsilon \frac{\partial T_F}{\partial t} + \rho_F u_F c_F \varepsilon \frac{\partial T_F}{\partial x} = \lambda_F \varepsilon \frac{\partial^2 T_F}{\partial x^2} + h_v (T_s - T_F), \text{ and} \tag{4.1}$$

$$\rho_s c_s (1-\varepsilon) \frac{\partial T_s}{\partial t} = \lambda_e \frac{\partial^2 T_s}{\partial x^2} - \frac{\partial q_r^n}{\partial x} - h_v (T_s - T_F) \ . \tag{4.2}$$

Where the local net radiative heat flux within the FP is expressed as:

$$q_r{}^n(\tau) = q_r{}^+(\tau) + q_r{}^-(\tau),$$

$$q_r{}^+(\tau) = 2\pi \left[I_0^+(\tau_{-x_{FP}}) E_3\left(\tau_{-x_{FP}} - \tau\right) + \int_{\tau_{-x_{FP}}}^{\tau} I_b(\tau') E_2(\tau' - \tau) d\tau \right], \quad \text{and} \tag{4.3}$$

$$q_r^-(\tau) = -2\pi\left[I_0^-(\tau_{x_{PC}})E_3(\tau_{x_{PC}}) + \int_0^{\tau_{x_{PC}}} I_b(\tau')E_2(\tau')d\tau' \right]E_3(\tau) - 2\pi\left[\int_{\tau}^{\tau_{-L}} I_b(\tau')E_2(\tau-\tau')d\tau' \right] \quad (4.4)$$

The Optical thickness in the FP section $\left(\tau_{-x_{FP}} \le \tau \le \tau_{-L}\right)$ is defined as $\tau = \kappa_{FP}(-L-x)$, which in PC section $\left(\tau_0 \le \tau \le \tau_{x_{PC}}\right)$ is defined as $\tau = \kappa_{PC}(x)$. The divergence of net radiative heat flux, $\frac{\partial q_r^n(\tau)}{\partial x}$ in equation (4.2), is evaluated from the integration of the radiant flux from each part of the porous medium, and is expressed as:

$$\begin{aligned}\frac{\partial q_r^n(\tau)}{\partial x} = &-2\kappa_{FP}\pi\left[-2I_b(\tau) + \int_{\tau_{-x_{FP}}}^{\tau_{-L}} I_b(\tau')E_1(|\tau-\tau'|)d\tau' + I_0^+(\tau_{-x_{FP}})E_2(\tau_{-x_{FP}}-\tau) \right] \\ &-2\kappa_{FP}\pi\left[I_0^-(\tau_{x_{PC}})E_3(\tau_{x_{PC}}) + \int_0^{\tau_{x_{PC}}} I_b(\tau')E_2(\tau')d\tau' \right]E_2(\tau) \\ &-2\kappa_{PC}\pi\left[I_0^-(\tau_{x_{PC}})E_2(\tau_{x_{PC}}) + I_b(\tau') - \int_0^{\tau_{x_{PC}}} I_b(\tau')E_1(\tau')d\tau' \right]E_3(\tau) .\end{aligned} \quad (4.5)$$

Where $I_b(\tau) = \frac{\sigma T_s^4(\tau)}{\pi}$,

$$\int_{\tau_{-x_{FP}}}^{\tau_{-L}} I_b(\tau')E_1(|\tau-\tau'|)d\tau' = \int_{\tau_{-x_{FP}}}^{\tau} I_b(\tau')E_1(\tau'-\tau)d\tau' + \int_{\tau}^{\tau_{-L}} I_b(\tau')E_1(\tau-\tau')d\tau'$$

and $E_n(\tau) = \int_0^1 \eta^{n-2}\exp(-\tau/\eta)d\eta$, $\quad n = 1, 2, 3.$

In the mixing chamber, the conservation equations for mass and energy are given by

$$\dot{m}_{mix} = \dot{m}_F + \dot{m}_a, \text{ and} \quad (4.6)$$

$$\dot{m}_{mix} h_{mix}(T_{mix}) = \dot{m}_F h_F(T_2) + \dot{m}_a h_a(T_{ao}) \,. \tag{4.7}$$

In the PC section, $0 \le x \le x_{PC}$ $(\tau_0 \le \tau \le \tau_{x_{PC}})$,

the conservation equation for energy of gas phase in PC is given by,

$$\rho_g c_g \varepsilon \frac{\partial T_g}{\partial t} + \rho_g u_g c_g \varepsilon \frac{\partial T_g}{\partial x} = \lambda_g \varepsilon \frac{\partial^2 T_g}{\partial x^2} + \varepsilon h_o w - h_v (T_g - T_s) \,. \tag{4.8}$$

The reaction rate is considered to follow the first-order Arrhenius equation,

$$w = A\rho(1-y)\exp(-E/RT) \,. \tag{4.9}$$

The conservation equation for the species of gas phase in PC is given by

$$\rho_g \varepsilon \frac{\partial y}{\partial t} + \rho_g u_g \varepsilon \frac{\partial y}{\partial x} = D\rho_g \varepsilon \frac{\partial^2 y}{\partial x^2} + \varepsilon w \,. \tag{4.10}$$

The conservation equation for the energy of solid phase in PC is given by

$$\rho_s c_s (1-\varepsilon) \frac{\partial T_s}{\partial t} = \lambda_e \frac{\partial^2 T_s}{\partial x^2} - \frac{\partial q_r^n}{\partial x} + h_v (T_g - T_s) \,. \tag{4.11}$$

Where the local net radiative heat flux within the PC is expressed as:

$$q_r^{\,n}(\tau) = q_r^{\,+}(\tau) + q_r^{\,-}(\tau),$$

$$q_r^{\,+}(\tau) = 2\pi \left[I_0^+(\tau_{-x_{FP}}) E_3(\tau_{-x_{FP}}) + \int_{\tau_{-x_{FP}}}^{\tau_{-L}} I_b(\tau') E_2(\tau') d\tau' \right] E_3(\tau) + 2\pi \left[\int_0^{\tau} I_b(\tau') E_2(\tau - \tau') d\tau' \right], \tag{4.12}$$

$$q_r^{\,-}(\tau) = -2\pi \left[I_0^-(\tau_{x_{PC}}) E_3(\tau_{x_{PC}} - \tau) + \int_{\tau}^{\tau_{x_{PC}}} I_b(\tau') E_2(\tau' - \tau) d\tau' \right]. \tag{4.13}$$

The divergence of the net radiative heat flux, $\frac{\partial q_r^n(\tau)}{\partial x}$ in equation (4.11), is expressed as:

$$\frac{\partial q_r^n(\tau)}{\partial x} = -2\pi\kappa_{PC}\left[I_0^+\left(\tau_{-x_{FP}}\right)E_3\left(\tau_{-x_{FP}}\right)+\int_{\tau_{-x_{FP}}}^{\tau_{-L}} I_b(\tau')E_2(\tau')d\tau'\right]E_2(\tau)$$
$$-2\pi\kappa_{PC}\left[-2I_b(\tau)+I_0^-\left(\tau_{x_{PC}}\right)E_2\left(\tau_{x_{PC}}-\tau\right)+\int_0^{\tau_{x_{PC}}} I_b(\tau')E_1\left(\left|\tau-\tau'\right|\right)d\tau'\right] .$$
$$-2\pi\kappa_{FP}\left[I_0^+\left(\tau_{-x_{FP}}\right)E_2\left(\tau_{-x_{FP}}\right)+I_b(\tau')+\int_{\tau_{-x_{FP}}}^{\tau_{-L}} I_b(\tau')E_1(\tau')d\tau'\right]E_3(\tau) .$$

(4.14)

Where, the last term of the equation (4.14) is defined as

$$\int_0^{\tau_{x_{PC}}} I_b(\tau')E_1\left(\left|\tau-\tau'\right|\right)d\tau' = \int_0^{\tau} I_b(\tau')E_1(\tau-\tau')d\tau' + \int_{\tau}^{\tau_{x_{PC}}} I_b(\tau')E_1(\tau'-\tau)d\tau' .$$

There are seven unknowns, T_F and T_s in the FP; $\dot{m}_{mix}$ and T_{mix} in the mixing chamber; T_g, T_s and y in the PC. There are seven equations to be solved.

4.1.4 Basic equations in case of preheated air

In this case, the PC is surrounded by the air jacket, which is used to preheated combustion air. Unlike in case of non-preheated air, a term of heat transfer from the hot gas in PC to the air jacket is considered in the gas energy equation. Moreover, the governing equations for the air jacket are also considered. In FP section and the mixing chamber, the considering equations like non-preheated air case. Therefore the governing equations in FP section and the mixing chamber do not shown again.

In the PC section, $0 \le x \le x_{PC}$ $\left(\tau_0 \le \tau \le \tau_{x_{PC}}\right)$

the conservation equation for energy of gas phase in PC is given by

$$\rho_g c_g \varepsilon \frac{\partial T_g}{\partial t} + \rho_g u_g c_g \varepsilon \frac{\partial T_g}{\partial x} = \lambda_g \varepsilon \frac{\partial^2 T_g}{\partial x^2} + \varepsilon h_o w - h_v (T_g - T_s) - \alpha U_w \left(T_g - T_w\right). \tag{4.15}$$

The last term of the right-hand side of equation (4.15) is heat transfer from the hot gas in PC to the wall, which preheats the air flowing in the air jacket. The reaction rate is considered to follow the first-order Arrhenius equation,

$$w = A\rho(1-y)\exp\left(-E/RT\right). \tag{4.16}$$

The conservation equation for the species of gas phase in PC is given by

$$\rho_g \varepsilon \frac{\partial y}{\partial t} + \rho_g u_g \varepsilon \frac{\partial y}{\partial x} = D\rho_g \varepsilon \frac{\partial^2 y}{\partial x^2} + \varepsilon w\,. \tag{4.17}$$

The conservation equation for the energy of solid phase in PC is given by

$$\rho_s c_s (1-\varepsilon) \frac{\partial T_s}{\partial t} = \lambda_e \frac{\partial^2 T_s}{\partial x^2} - \frac{\partial q_r^n}{\partial x} + h_v (T_g - T_s)\,. \tag{4.18}$$

Where the local net radiative heat flux within the PC is expressed as:

$$q_r{}^n(\tau) = q_r{}^+(\tau) + q_r{}^-(\tau),$$

$$q_r{}^+(\tau) = 2\pi\left[I_0^+(\tau_{-x_{FP}}) E_3\left(\tau_{-x_{FP}}\right) + \int_{\tau_{-x_{FP}}}^{\tau_{-L}} I_b(\tau') E_2(\tau') d\tau' \right] E_3(\tau) + 2\pi\left[\int_0^{\tau} I_b(\tau') E_2(\tau - \tau') d\tau' \right], \tag{4.19}$$

$$q_r^-(\tau) = -2\pi\left[I_0^-(\tau_{x_{PC}})E_3(\tau_{x_{PC}} - \tau) + \int_{\tau}^{\tau_{x_{PC}}} I_b(\tau')E_2(\tau' - \tau)d\tau' \right]. \qquad (4.20)$$

The divergence of the net radiative heat flux, $\frac{\partial q_r^n(\tau)}{\partial x}$ in equation (11), is expressed as:

$$\begin{aligned}\frac{\partial q_r^n(\tau)}{\partial x} = &-2\pi\kappa_{PC}\left[I_0^+(\tau_{-x_{FP}})E_3(\tau_{-x_{FP}}) + \int_{\tau_{-x_{FP}}}^{\tau_{-L}} I_b(\tau')E_2(\tau')d\tau' \right]E_2(\tau) \\ &-2\pi\kappa_{PC}\left[-2I_b(\tau) + I_0^-(\tau_{x_{PC}})E_2(\tau_{x_{PC}} - \tau) + \int_0^{\tau_{x_{PC}}} I_b(\tau')E_1(|\tau - \tau'|)d\tau' \right] \\ &-2\pi\kappa_{FP}\left[I_0^+(\tau_{-x_{FP}})E_2(\tau_{-x_{FP}}) + I_b(\tau') + \int_{\tau_{-x_{FP}}}^{\tau_{-L}} I_b(\tau')E_1(\tau')d\tau' \right]E_3(\tau)\ .\end{aligned} \qquad (4.21)$$

Where, the last term of the equation (4.21) is defined as

$$\int_0^{\tau_{x_{PC}}} I_b(\tau')E_1(|\tau - \tau'|)d\tau' = \int_0^{\tau} I_b(\tau')E_1(\tau - \tau')d\tau' + \int_{\tau}^{\tau_{x_{PC}}} I_b(\tau')E_1(\tau' - \tau)d\tau'.$$

There are nine unknowns, T_F and T_s in the FP: $\dot{m}_{mix}$, T_{mix} and T_{ao} in the mixing chamber, T_g, T_s, y and T_w in the PC, but there are seven equations to be solved. Thus, another two equations are needed in the air jacket, which are shown in equations (4.22) and (4.23).

In the air jacket, heat transfer from the hot gas in PC to the wall is equal to heat convection from the wall to the combustion air in the air jacket, which in turn is equal to an increase in the sensible heat of the combustion air flowing in the air jacket. Therefore, we obtain

$$\int_0^{x_{PC}} U_w(T_g - T_w)(2\pi r_{PC})dx = h_w A_w \Delta T_{ln}, \qquad (4.22)$$

$$\dot{m}_a c_a dT_a = h_w (T_w - T_a) dA . \tag{4.23}$$

where $\Delta T_{ln} = \dfrac{\Delta T_o - \Delta T_i}{\ln(\Delta T_o / \Delta T_i)}$, $\Delta T_o = T_w - T_{ao}$, $\Delta T_i = T_w - T_{ai}$ and $T_{ai} = T_0$.

T_{ao}, in terms of T_w and T_{ai}, can be determined by integrating equation (4.23) over the surface area of the wall. Substituting T_{ao} into equation (4.22) gives the following equation, $T_w = \dfrac{C \int_0^{x_{PC}} T_g(x) dx + (B-1) T_{ai}}{D}$, where B, C, and D are defined as $B = \exp(-2\pi r_{PC} x_{PC} h_w / \dot{m}_a c_a)$, $C = 2\pi r_{PC} U_w \ln B / (h_w A_w)$ and $D = C + B x_{PC} - 1$.

In the combustion model using gaseous fuel, the fuel flow rate in the FP is small compared with the combustion air, the heat transfer between the gas and solid phases is not significantly changed with varying firing rates. Thus, the volumetric heat transfer in FP is considered constant and is equal to 9.1 × 10^5 W/m^3·K (Yoshizawa et al. 1988). The correlation for volumetric heat transfer coefficient Nu_v used in PC is given by the following correlation (Wakao et al. 1979):

$$Nu_v = h_v d_p^2 / \lambda_g = A_{sf} d_P \left(2 + 1.1 Re_{d_P}^{0.6} Pr^{1/3}\right), \tag{4.24}$$

where, the specific surface area is defined as $A_{sf} = \dfrac{6(1-\varepsilon)}{d_P}$.

Because the porous structure of PC is a packed bed of randomly arranged spheres, the effective thermal conductivity is difficult to estimate. This work uses the relation $\lambda_e = (1-\varepsilon)\lambda_s$ when continuous structure of the PC is assumed. The boundary conditions are summarized in Table 4.1. The initial conditions for these simulations are obtained from experimental data. The physical properties of gas, based on the average temperature at each zone, are constant. All the properties used are summarized in Table 4.2.

Table 4.1 Boundary conditions.

FP Section		PC Section	
$x = -x_{FP}$	$x = -L$	$x = 0$	$x = x_{PC}$
$T_F = T_0$	$\frac{\partial T_F}{\partial x} = 0$	$T_g = T_{mix}$	$\frac{\partial T_g}{\partial x} = 0$
$\frac{\partial T_s}{\partial x} = 0$	$\frac{\partial T_s}{\partial x} = 0$	$\frac{\partial T_s}{\partial x} = 0$	$\frac{\partial T_s}{\partial x} = 0$
-	-	$y = y_0$	$\frac{\partial y}{\partial x} = 0$
$I_0^+(\tau_{-x_{FP}}) = \frac{\sigma T_0^4}{\pi}$	$I^-(\tau_{-L}) = I_0^-(\tau_{x_{PC}})E_3(\tau_{x_{PC}}) + \int_0^{\tau_{x_{PC}}} I_b(\tau')E_2(\tau')d\tau'$	$I^+(\tau_0) = I_0^+(\tau_{-x_{FP}})E_3(\tau_{-x_{FP}}) + \int_{\tau_{-x_{FP}}}^{\tau_{-L}} I_b(\tau')E_2(\tau')d\tau'$	$I_0^-(\tau_{x_{PC}}) = \frac{\sigma T_0^4}{\pi}$

Table 4.2 Solid property data used for simulations.

Properties	**FP**	**PC**	**Unit**
Porosity, ε	0.61	0.36	-
Effective thermal conductivity of solid, λ_e	12.1	1.8	$W.m^{-1}.K$
Volumetric heat transfer coefficient, h_v	Yoshizawa et al. 1988	Wakao et al. 1979	$W.m^{-3}.K$
Absorption coefficient, κ	1750	71	m^{-1}
Apparent density, $\rho_s(1-\varepsilon)$	2510	1714	kg/m^3
Specific heat, c_s	3120	775	$J.kg^{-1}.K^{-1}$

The conservation equations of species and energy both in FP and PC are discretized by finite differential approximations. An implicit difference scheme is adopted with respect to time, and a central difference scheme is adopted with respect to space. The convergence criteria for numerical computation of all variables are set to 10^{-6}.

Time step and mesh size were tested using different value. As a compromise between an accuracy and computational time, 100 uniform grid points both in the PE and PC, and 0.1 s time steps are selected. The final error in the energy balance is usually less than 1%.

4.2 Solution procedures

The conservation equations of species and energy are reduced to dimensionless form, which allow a universal application of the solution. Later the dimensionless equations are solved numerically by the method of characteristics. The dimensionless terms using in this model, are as follows.

In the FP section, $-x_{FP} \le x \le -L \ \left(\tau_{-x_{FP}} \le \tau \le \tau_{-L}\right)$,

$$\mathrm{Re}_{FP} = \frac{\rho_F u x_{FP}}{\mu_F},\ \mathrm{CD} = (1-\varepsilon)\frac{\rho_F u x_{FP}}{\mu_F},\ \Gamma = \frac{\rho_s c_s}{\rho_F c_F},\ \mathrm{Pr} = \frac{\mu_F c_F}{\lambda_F},\ \mathrm{Mp} = \frac{h_v x_{FP}^2}{\lambda_F},$$

$$\tau_{FP} = \kappa_{FP} x_{FP},\ \mathrm{Nr} = \frac{\kappa_{FP}\lambda_F}{4\sigma T_0^3},\ \mathrm{Le} = \frac{\lambda_F}{D\rho_F c_F},\ X = \frac{x}{x_{FP}},\ \theta_F = \frac{T_F}{T_0},\ \theta_s = \frac{T_s}{T_0},\ H = \frac{q_r}{4\sigma T_0^4},$$

$$S = \frac{ut}{X_{FP}},\ J = \frac{\pi I}{\sigma T_s^4}$$

In the PC section, $0 \le x \le x_{PC} \ \left(\tau_0 \le \tau \le \tau_{x_{PC}}\right)$,

$$\mathrm{Re}_{PC} = \frac{\rho_g u x_{PC}}{\mu_g},\ \mathrm{CD} = (1-\varepsilon)\frac{\rho_g u x_{PC}}{\mu_g},\ \Gamma = \frac{\rho_s c_s}{\rho_g c_g},\ \mathrm{Pr} = \frac{\mu_g c_g}{\lambda_g},\ \mathrm{Mp} = \frac{h_v x_{PC}^2}{\lambda_g},$$

$$\tau_{PC} = \kappa_{PC} x_{PC},\ \mathrm{Nr} = \frac{\kappa_{PC}\lambda_g}{4\sigma T_0^3},\ \mathrm{Le} = \frac{\lambda_g}{D\rho_g c_g},\ \mathrm{Rs} = \frac{x_{PC}^2 \rho_g A}{\mu_g},\ X = \frac{x}{x_{PC}},\ H = \frac{q_r}{4\sigma T_0^4},$$

$$\theta_g = \frac{T_g}{T_0},\ \theta_s = \frac{T_s}{T_0},\ S = \frac{ut}{x_{PC}},\ \mathrm{RR} = \frac{\mathrm{Rs.Pr.w}}{\mathrm{Re}_{PC}},\ \mathrm{Ka} = \frac{\alpha U_w}{h_v},\ J = \frac{\pi I}{\sigma T_s^4}$$

The dimensionless forms are approximated by finite difference expressions. Fixing a mass flow rate both in FP and PC are considered. In case of non-preheated air, in FP, T_F and T_s are calculated. In PC, $\dot{m}_{mix}$, T_{mix}, T_g, T_s, and y are solved. In case of preheated air, in PC, has addition term (heat transfer from the hot gas in PC to the wall). Thus, T_{ao} and T_w are also calculated.

4.2.1 Dimensionless form of governing equation

Using dimensionless parameter, the governing equations in FP section, $-x_{FP} \le x \le -L \quad \left(\tau_{-x_{FP}} \le \tau \le \tau_{-L}\right)$ are normalized. The dimensionless governing equations for energy of gas and solid phase are

$$\varepsilon\frac{\partial\theta_F}{\partial S}+\varepsilon\frac{\partial\theta_F}{\partial X}=\left(\frac{\varepsilon}{Re_{FP}\,Pr}\right)\frac{\partial^2\theta_F}{\partial X^2}+\left(\frac{Mp}{Re_{FP}\,Pr}\right)(\theta_s-\theta_F),\ \text{and} \tag{4.25}$$

$$(1-\varepsilon)\Gamma\frac{\partial\theta_s}{\partial S}=\left(\frac{CD}{Re_{FP}\,Pr}\right).\left(\frac{\partial^2\theta_s}{\partial X^2}\right)-\left(\frac{\tau_{FP}^2}{Re_{FP}\,Pr\,Nr}\right).\left(\frac{\partial H}{\partial\tau}\right)-\left(\frac{Mp}{Re_{FP}\,Pr}\right)(\theta_s-\theta_F) \tag{4.26}$$

Where the dimensionless local net radiative heat flux within the FP is expressed as:

$$H_r^{\,n}(\tau)=H_r^{\,+}(\tau)+H_r^{\,-}(\tau),$$

$$H_r^{\,+}(\tau)=\frac{1}{2}\left[J_0^+(\tau_{-x_{FP}})E_3\left(\tau_{-x_{FP}}-\tau\right)+\int_{\tau_{-x_{FP}}}^{\tau}\theta_s^4(\tau')E_2(\tau'-\tau)\,d\tau\right],\quad\text{and} \tag{4.27}$$

$$\begin{aligned}H_r^{\,-}(\tau)=&-\frac{1}{2}\left[J_0^-(\tau_{x_{PC}})E_3\left(\tau_{x_{PC}}\right)+\int_0^{\tau_{x_{PC}}}\theta_s^4(\tau')E_2(\tau')\,d\tau'\right]E_3(\tau)\\&-\frac{1}{2}\left[\int_{\tau}^{\tau_{-L}}\theta_s^4(\tau')E_2(\tau-\tau')\,d\tau'\right].\end{aligned} \tag{4.28}$$

The divergence of the dimensionless net radiative heat flux is expressed as:

$$\begin{aligned}\frac{\partial H_r^{\,n}(\tau)}{\partial\tau}=&-\frac{1}{2}\left[-2J_b(\tau)+\int_{\tau_{-x_{FP}}}^{\tau_{-L}}\theta_s^4(\tau')E_1\left(|\tau-\tau'|\right)d\tau'+J_0^+\left(\tau_{-x_{FP}}\right)E_2\left(\tau_{-x_{FP}}-\tau\right)\right]\\&-\frac{1}{2}\left[J_0^-\left(\tau_{x_{PC}}\right)E_3\left(\tau_{x_{PC}}\right)+\int_0^{\tau_{x_{PC}}}\theta_s^4(\tau')E_2(\tau')\,d\tau'\right]E_2(\tau)\\&-\frac{1}{2}\left[J_0^-\left(\tau_{x_{PC}}\right)E_2\left(\tau_{x_{PC}}\right)+J_b(\tau')+\int_0^{\tau_{x_{PC}}}\theta_s^4(\tau')E_1(\tau')\,d\tau'\right]E_3(\tau).\end{aligned} \tag{4.29}$$

In the PC section, $0 \le x \le x_{PC}$ $\left(\tau_0 \le \tau \le \tau_{x_{PC}}\right)$, the conservation equation for energy of gas phase in PC in dimensionless form is given by

$$\frac{\partial \theta_g}{\partial S} + \frac{\partial \theta_g}{\partial X} = \left(\frac{1}{Re_{x_{PC}}\,Pr}\right)\frac{\partial^2 \theta_g}{\partial X^2} + \left(\frac{H_o}{Re_{x_{PC}}\,Pr}\right)RR(i) - \left(\frac{Mp}{\varepsilon\, Re_{x_{PC}}\,Pr}\right)(\theta_g - \theta_s) - \left(\frac{KaMp}{\varepsilon\, Re_{x_{PC}}\,Pr}\right)\left(\theta_g - \theta_w\right). \tag{4.30}$$

The dimensionless parameter Ka in the last term of the right-hand side of equation (4.30) is defined as

$$Ka = \frac{\alpha U_w}{h_v}.$$

Where in case of non-preheated air, $Ka = 0$ and

in case of preheated air, $Ka \neq 0$

$$\theta_w = \frac{T_w}{T_0}.$$

The dimensionless conservation equation for the species of gas phase in PC is given by

$$\frac{\partial Y}{\partial S} + \frac{\partial Y}{\partial X} = \left(\frac{1}{Re_{PC}\,Le\,Pr}\right)\frac{\partial^2 Y}{\partial X^2} + \left(\frac{1}{Re_{PC}\,Pr}\right)RR(i). \tag{4.31}$$

The conservation equation for the energy of solid phase in PC in dimensionless form is given by

$$\Gamma(1-\varepsilon)\frac{\partial \theta_s}{\partial S} = \left(\frac{CD}{Re_{PC}\,Pr}\right)\frac{\partial^2 \theta_s}{\partial x^2} - \left(\frac{\tau_{PC}^2}{Re_{PC}\,Pr\,Nr}\right)\frac{\partial H}{\partial \tau} + \left(\frac{Mp}{Re_{PC}\,Pr}\right)(\theta_g - \theta_s). \tag{4.32}$$

Where the local net radiative heat flux within the PC is expressed as:

$$H_r^{\,n}(\tau) = H_r^{\,+}(\tau) + H_r^{\,-}(\tau),$$

$$H_r^+(\tau)=\frac{1}{2}\left[J_0^+(\tau_{-x_{FP}})E_3\left(\tau_{-x_{FP}}\right)+\int_{\tau_{-x_{FP}}}^{\tau_{-L}}\theta_s^4(\tau')E_2(\tau')d\tau'\right]E_3(\tau) + \frac{1}{2}\left[\int_0^{\tau}\theta_s^4(\tau')E_2(\tau-\tau')d\tau'\right], \quad (4.33)$$

$$H_r^-(\tau)=-\frac{1}{2}\left[J_0^-(\tau_{x_{PC}})E_3\left(\tau_{x_{PC}}-\tau\right)+\int_{\tau}^{\tau_{x_{PC}}}\theta_s^4(\tau')E_2(\tau'-\tau)d\tau'\right]. \quad (4.34)$$

The dimensionless divergence of the net radiative heat flux, $\frac{\partial H_r^n(\tau)}{\partial\tau}$ is expressed as:

$$\frac{\partial H_r^n(\tau)}{\partial\tau}=-\frac{1}{2}\left[J_0^+\left(\tau_{-x_{FP}}\right)E_3\left(\tau_{-x_{FP}}\right)+\int_{\tau_{-x_{FP}}}^{\tau_{-L}}\theta_s^4(\tau')E_2(\tau')d\tau'\right]E_2(\tau) -\frac{1}{2}\left[-2J_b(\tau)+J_0^-\left(\tau_{x_{PC}}\right)E_2\left(\tau_{x_{PC}}-\tau\right)+\int_0^{\tau_{x_{PC}}}\theta_s^4(\tau')E_1\left(\left|\tau-\tau'\right|\right)d\tau'\right] \quad (4.35)$$
$$-\frac{1}{2}\left[J_0^+\left(\tau_{-x_{FP}}\right)E_2\left(\tau_{-x_{FP}}\right)+J_b(\tau')+\int_{\tau_{-x_{FP}}}^{\tau_{-L}}\theta_s^4(\tau')E_1(\tau')d\tau'\right]E_3(\tau).$$

Next step, the governing equation of energy and species in dimensionless form both in FP and PC zones are discretized by differential approximations

4.2.2 Differential approximations

The numerical solution to the partial differential equation is an approximation to the exact solution that is obtained using a discrete representation to the partial differential equation at the grid points i in the discrete spatial mesh at considering time level j. A standard backward finite difference approximation for the first-order derivatives are applied into the governing equation (refer figure 4.3).

$$\frac{\partial\theta_i^j}{\partial S}=\frac{\theta_i^j-\theta_i^{j-1}}{\Delta S}, \quad (4.36)$$

$$\frac{\partial \theta_i^j}{\partial X} = \frac{\theta_{i+1}^j - \theta_i^j}{\Delta X}. \tag{4.37}$$

The central difference approximation of second-order derivative using in this model is

$$\frac{\partial^2 \theta_i^j}{\partial X^2} = \frac{\theta_{i+1}^j - 2\theta_i^j + \theta_{i-1}^j}{\Delta X^2}. \tag{4.38}$$

The governing equations both in FP and PC are discretized by using equation (4.36), (4.37), and (4.38) and rearranged in order to obtain a numerical solution through the iterative process. Simple form of equations are prepared for solving by numerical method are expressed following.

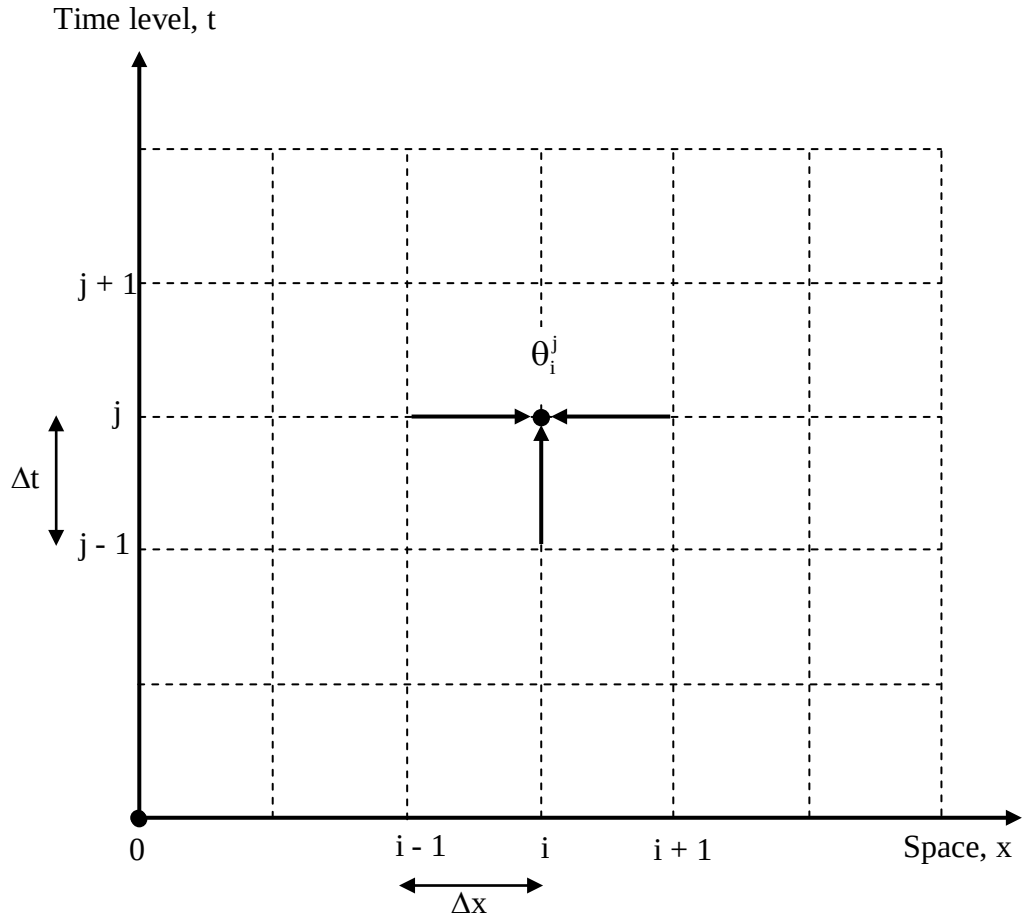

Figure 4.3 Space-time grids.

In FP section, $-x_{FP} \le x \le -L \quad \left(\tau_{-x_{FP}} \le \tau \le \tau_{-L}\right)$

$$\left(\theta_F\right)_i^j = \frac{1}{\left(\frac{1}{\Delta S}+\frac{1}{\Delta X}+\frac{2}{Re_{FP}\,Pr\,\Delta X^2}+\frac{Mp}{\varepsilon\,Re_{FP}\,Pr}\right)}\cdot\left\{\frac{\left(\theta_F\right)_i^{j-1}}{\Delta S}+\frac{\left(\theta_F\right)_{i-1}^{j}}{\Delta X}\right.$$
$$\left.\left(\frac{1}{Re_{FP}\,Pr\,\Delta X^2}\right)\left[\left(\theta_F\right)_{i+1}^{j}+\left(\theta_F\right)_{i-1}^{j}\right]+\left(\frac{Mp}{\varepsilon\,Re_{FP}\,Pr}\right)\left(\theta_s\right)_i^j\right\} \tag{4.39}$$

$$\left(\theta_s\right)_i^j = \frac{1}{\left(\frac{\Gamma(1-\varepsilon)}{\Delta S}+\frac{2CD}{Re_{FP}\,Pr\,\Delta X^2}+\frac{Mp}{Re_{FP}\,Pr}\right)}\cdot\left\{\left(\frac{\Gamma(1-\varepsilon)}{\Delta S}\right)\left(\theta_s\right)_i^{j-1}+\frac{\left(\theta_F\right)_{i-1}^{j}}{\Delta X}\right.$$
$$\left.\left(\frac{CD}{Re_{FP}\,Pr\,\Delta X^2}\right)\left[\left(\theta_s\right)_{i+1}^{j}+\left(\theta_s\right)_{i-1}^{j}\right]+\left(\frac{Mp}{Re_{FP}\,Pr}\right)\left(\theta_F\right)_i^j-\left(\frac{\tau_{FP}^2}{Re_{FP}\,Pr\,\Delta X^2}\right)\left(\frac{\partial H}{\partial\tau}\right)\right\}. \tag{4.40}$$

In the PC section, $0 \le x \le x_{PC} \quad \left(\tau_0 \le \tau \le \tau_{x_{PC}}\right)$

$$\left(\theta_g\right)_i^j = \frac{1}{\left(\frac{1}{\Delta S}+\frac{1}{\Delta X}+\frac{2}{Re_{PC}\,Pr\,\Delta X^2}+\frac{Mp}{\varepsilon\,Re_{PC}\,Pr}+\frac{KaMp}{\varepsilon\,Re_{PC}\,Pr}\right)}\cdot\left\{\frac{\left(\theta_g\right)_i^{j-1}}{\Delta S}+\frac{\left(\theta_g\right)_{i-1}^{j}}{\Delta X}\right.$$
$$\left(\frac{1}{Re_{PC}\,Pr\,\Delta X^2}\right)\left[\left(\theta_g\right)_{i+1}^{j}+\left(\theta_g\right)_{i-1}^{j}\right]+\left(\frac{Ho}{Re_{PC}\,Pr}\right)RR_i^j+\left(\frac{Mp}{\varepsilon\,Re_{PC}\,Pr}\right)\left(\theta_s\right)_i^j$$
$$\left.+\left(\frac{KaMp}{\varepsilon\,Re_{PC}\,Pr}\right)\theta_w\right\} \tag{4.41}$$

$$Y_i^j = \frac{1}{\left(\frac{1}{\Delta S}+\frac{1}{\Delta X}+\frac{2}{Re_{PC}\,Le\,Pr\,\Delta X^2}+ARR_i^j\right)}\cdot\left\{\left(\frac{Y_i^j}{\Delta S}\right)+\frac{Y_{i-1}^j}{\Delta X}\right.$$
$$\left.\left(\frac{1}{Re_{PC}\,Le\,Pr\,\Delta X^2}\right)\left[Y_{i+1}^j+Y_{i-1}^j\right]+ARR_i^j\right\} \tag{4.42}$$

Where, $ARR_i^j = \dfrac{Rs.\exp\left[-E_a/\left(\theta_g\right)_i^j\right]}{Re_{PC}}$.

$$\left(\theta_s\right)_i^j = \frac{1}{\left(\dfrac{\Gamma\left(1-\varepsilon\right)}{\Delta S} + \dfrac{2CD}{Re_{PC}\,Pr\,\Delta X^2} + \dfrac{Mp}{Re_{PC}\,Pr}\right)} \cdot \left\{ \left(\frac{\Gamma\left(1-\varepsilon\right)}{\Delta S}\right)\left(\theta_s\right)_i^{j-1} + \frac{\left(\theta_g\right)_{i-1}^j}{\Delta X} \right.$$
$$\left. \left(\frac{CD}{Re_{PC}\,Pr\,\Delta X^2}\right)\left[\left(\theta_s\right)_{i+1}^j + \left(\theta_s\right)_{i-1}^j\right] + \left(\frac{Mp}{Re_{PC}\,Pr}\right)\left(\theta_g\right)_i^j - \left(\frac{\tau_{PC}^2}{Re_{PC}\,Pr\,\Delta X^2}\right)\cdot\left(\frac{\partial H}{\partial \tau}\right) \right\} \tag{4.43}$$

Non-dimensional equations for species and energy equations can be solved numerically along the characteristics. The model accuracy is examined by local and global energy balance equations are given in the following sections.

4.2.3 Non-dimensional energy equations

The local energy balance equations both in FP and PC can be expressed in the dimensionless forms given in equation (4.44), (4.45), (4.46), and (4.47)

In FP section, $-x_{FP} \le x \le -L \;\; \left(\tau_{-x_{FP}} \le \tau \le \tau_{-L}\right)$

The local energy balance equation for gas and solid phase are as following

$$\left(\frac{\varepsilon}{Re_{FP}\,Pr}\right)\frac{\partial^2\theta_F}{\partial X^2} + \left(\frac{Mp}{Re_{FP}\,Pr}\right)(\theta_s - \theta_F) - \varepsilon\frac{\partial\theta_F}{\partial X} = 0, \text{ and} \tag{4.44}$$

$$\left(\frac{CD}{Re_{FP}\,Pr}\right)\cdot\left(\frac{\partial^2\theta_s}{\partial X^2}\right) - \left(\frac{\tau_{FP}^2}{Re_{FP}\,Pr\,Nr}\right)\cdot\left(\frac{\partial H}{\partial \tau}\right) - \left(\frac{Mp}{Re_{FP}\,Pr}\right)(\theta_s - \theta_F) = 0 \tag{4.45}$$

In the PC section, $0 \le x \le x_{PC}$ $\left(\tau_0 \le \tau \le \tau_{x_{PC}}\right)$

The local energy balance equation for gas and solid phase are as following

$$\left(\frac{\varepsilon}{Re_{x_{PC}}\,Pr}\right)\frac{\partial^2\theta_g}{\partial X^2}+\left(\frac{\varepsilon H_o}{Re_{x_{PC}}\,Pr}\right)RR(i)-\left(\frac{Mp}{Re_{x_{PC}}\,Pr}\right)(\theta_g-\theta_s) -\varepsilon\frac{\partial\theta_g}{\partial X}-\left(\frac{KaMp}{Re_{x_{PC}}\,Pr}\right)\left(\theta_g-\theta_w\right)=0 \tag{4.46}$$

$$\left(\frac{CD}{Re_{PC}\,Pr}\right)\frac{\partial^2\theta_s}{\partial x^2}-\left(\frac{\tau_{PC}^2}{Re_{PC}\,Pr\,Nr}\right)\frac{\partial H}{\partial\tau}+\left(\frac{Mp}{Re_{PC}\,Pr}\right)(\theta_g-\theta_s)=0. \tag{4.47}$$

The global energy balance for the system is expressed

$$\left[\int_1^N\left\{\left(\frac{\varepsilon}{Re_{FP}\,Pr}\right)\frac{\partial^2\theta_F}{\partial X^2}+\cancel{\left(\frac{Mp}{Re_{FP}\,Pr}\right)}(\theta_s-\theta_F)-\varepsilon\frac{\partial\theta_F}{\partial X} +\left(\frac{CD}{Re_{FP}\,Pr}\right)\cdot\left(\frac{\partial^2\theta_s}{\partial X^2}\right)-\left(\frac{\tau_{FP}^2}{Re_{FP}\,Pr\,Nr}\right)\cdot\left(\frac{\partial H}{\partial\tau}\right)-\cancel{\left(\frac{Mp}{Re_{FP}\,Pr}\right)}(\theta_s-\theta_F)\right\}dX\right]_{FP} +\left[\int_1^N\left\{\left(\frac{\varepsilon}{Re_{x_{PC}}\,Pr}\right)\frac{\partial^2\theta_g}{\partial X^2}+\left(\frac{\varepsilon H_o}{Re_{x_{PC}}\,Pr}\right)RR(i)-\cancel{\left(\frac{Mp}{Re_{x_{PC}}\,Pr}\right)}(\theta_g-\theta_s)-\varepsilon\frac{\partial\theta_g}{\partial X} -\left(\frac{KaMp}{Re_{x_{PC}}\,Pr}\right)\left(\theta_g-\theta_w\right)+\left(\frac{CD}{Re_{PC}\,Pr}\right)\frac{\partial^2\theta_s}{\partial x^2}-\left(\frac{\tau_{PC}^2}{Re_{PC}\,Pr\,Nr}\right)\frac{\partial H}{\partial\tau} +\cancel{\left(\frac{Mp}{Re_{PC}\,Pr}\right)}(\theta_g-\theta_s)\right\}dX\right]_{PC}=0. \tag{4.48}$$

The rearrange global energy balance is

$$\left[\int_1^N\left\{\left(\frac{\varepsilon}{\mathrm{Re_{FP}\,Pr}}\right)\frac{\partial^2\theta_F}{\partial X^2}-\varepsilon\frac{\partial\theta_F}{\partial X}+\left(\frac{\mathrm{CD}}{\mathrm{Re_{FP}\,Pr}}\right).\left(\frac{\partial^2\theta_s}{\partial X^2}\right)\right.\right.$$
$$\left.\left.-\left(\frac{\tau_{FP}^2}{\mathrm{Re_{FP}\,Pr\,Nr}}\right).\left(\frac{\partial H}{\partial\tau}\right)\right\}dX\right]_{FP}$$
$$+\left[\int_1^N\left\{\left(\frac{\varepsilon}{\mathrm{Re_{x_{PC}}\,Pr}}\right)\frac{\partial^2\theta_g}{\partial X^2}+\left(\frac{\varepsilon H_o}{\mathrm{Re_{x_{PC}}\,Pr}}\right)\mathrm{RR(i)}-\varepsilon\frac{\partial\theta_g}{\partial X}-\left(\frac{\mathrm{KaMp}}{\mathrm{Re_{x_{PC}}\,Pr}}\right)\left(\theta_g-\theta_w\right)\right.\right.$$
$$\left.\left.+\left(\frac{\mathrm{CD}}{\mathrm{Re_{PC}\,Pr}}\right)\frac{\partial^2\theta_s}{\partial x^2}-\left(\frac{\tau_{PC}^2}{\mathrm{Re_{PC}\,Pr\,Nr}}\right)\frac{\partial H}{\partial\tau}\right\}dX\right]_{PC}=0. \tag{4.49}$$

This problem has not formula for the exact solution; an iteration method is used to solve. The approximation method starts from an initial guess, which is provided by the experimental data. Later is computing step by step (in general better and better) approximations of an unknown solution until the answer can be accepted.

Three famous iterative methods are fixed-point iteration, Secant method, and Newton-Raphson's method for solving equation f(x) = 0. This thesis the Newton-Raphson's method is used because of its simplicity and great speed. In general, iteration methods are easy to program because the computational operations are the same in each step and just the data will change from step to step. The numerical solution is implemented in FORTRAN taking the numerical convergence and stability into account. The one-dimensional problem for the domain $-x_{FP} \le x \le x_{PC}$ that is illustrated in figure 4.1 is solved.

4.3 Definitions of heat recirculation and radiant output efficiency

A single layer burner (SLB) in this study refers to a premixed combustion in a porous medium burner, which has the same physical properties as that of the PC of the LMPB. Fig. 4.4 shows the preheat zone of the SLB, which begins where the gas temperature has increased by 1% of its original inlet value, section x_1, and ends where the gas and solid temperature are equal, section x_2 (Barra and Ellzey 2004). The heat recirculation efficiency is the measurement of the amount of heat

transferred to the gas in the preheat zone. For the SLB, the heat recirculation efficiency is defined as

$$(\eta_{rec})_{SLB} = \left[\frac{\text{solid-to-gas convection in preheat zone}}{\text{FR}}\right] \quad (4.50)$$

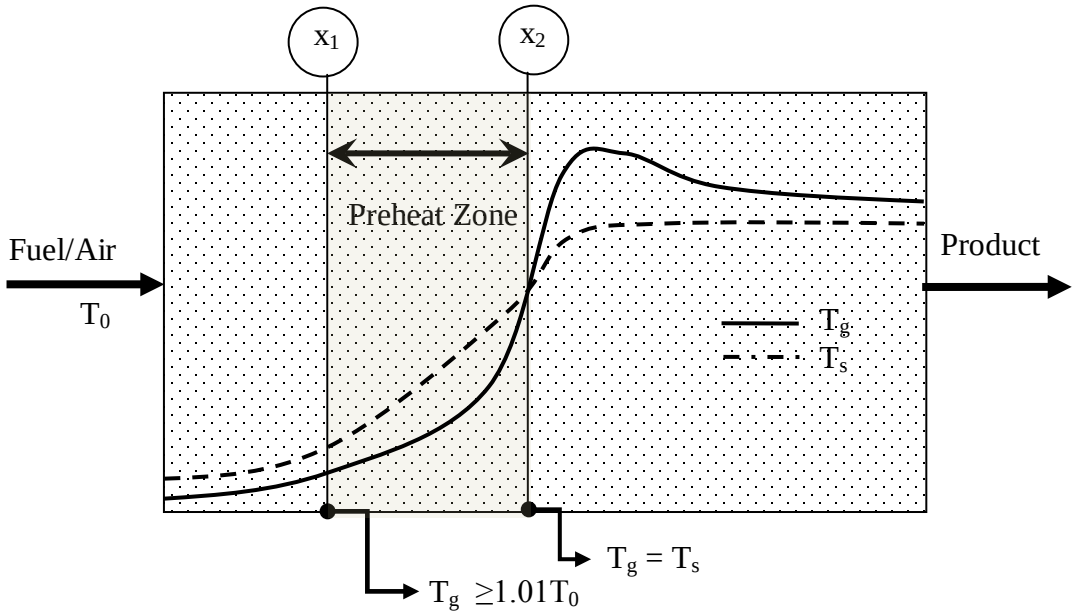

Figure 4.4 Definition of preheat zone of SLB.

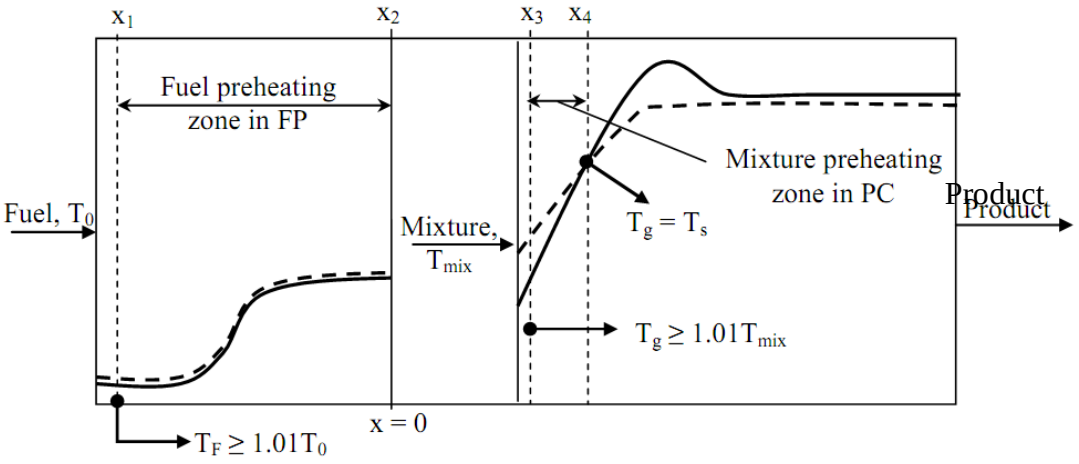

Figure 4.5 Definition of preheat zone of LMPB in case of non-preheated air.

The LMPB in case of non-preheated has two preheating zone in porous FP and PC as show in Fig.4.5. While in case of preheated air consists of three preheating zone

in porous FP, porous PC and air jacket as show in Fig.4.6. The heat recirculation efficiency in case of non-preheated air is defined as

$$(\eta_{rec})_{NPB} = \frac{\left[\int_{x_1}^{x_2} h_v (T_s - T_F)dV + \int_{x_3}^{x_4} h_v (T_s - T_g)dV\right]}{FR}. \quad (4.51)$$

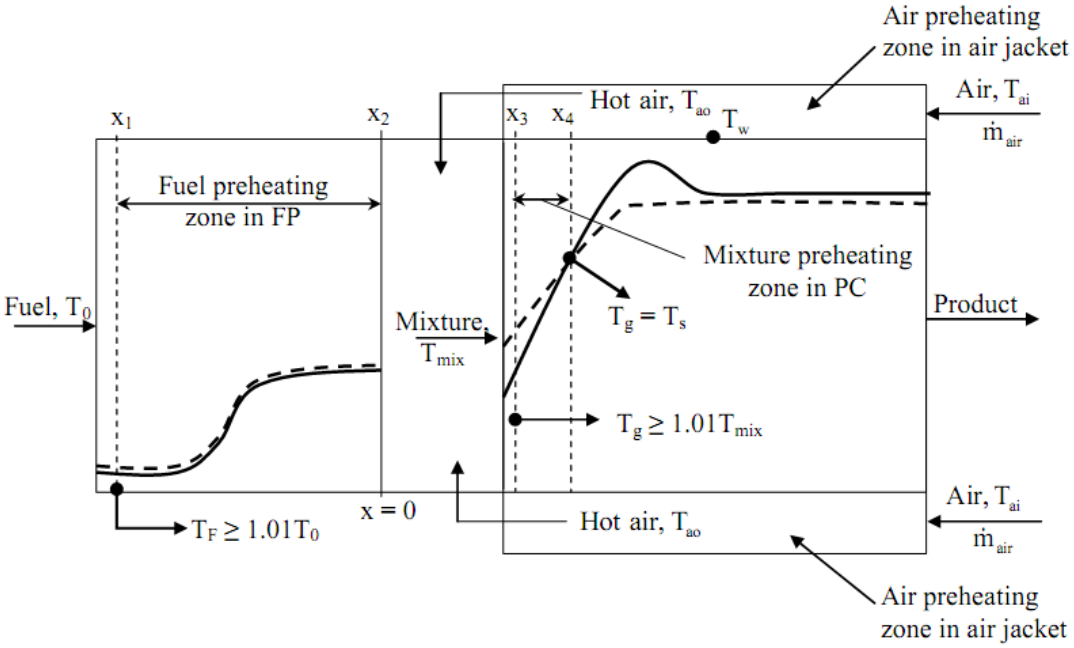

Figure 4.6 Definition of preheat zone of LMPB in case of preheated air.

The heat recirculation efficiency in case of preheated air is defined as

$$(\eta_{rec})_{NPB} = \frac{\left[\int_{x_1}^{x_2} h_v (T_s - T_F)dV + \dot{m}_a c_a (T_{ao} - T_{ai}) + \int_{x_3}^{x_4} h_v (T_s - T_g)dV\right]}{FR}. \quad (4.52)$$

Where, x_1 and x_3 are positions, at which the gas temperature has increased by 1% of its original inlet value in the FP and the PC, respectively. x_2 is an outlet of the FP and x_4 is a position, where the gas and solid temperature are equal in the PC.

The radiant output efficiency for both the SLB and the LMPB is defined as

$$\eta_{rad} = \frac{\text{heat radiates out the exit of the burner}}{FR}. \quad (4.53)$$

4.4 Results and discussion in case of non-preheated air

4.4.1 Model validation

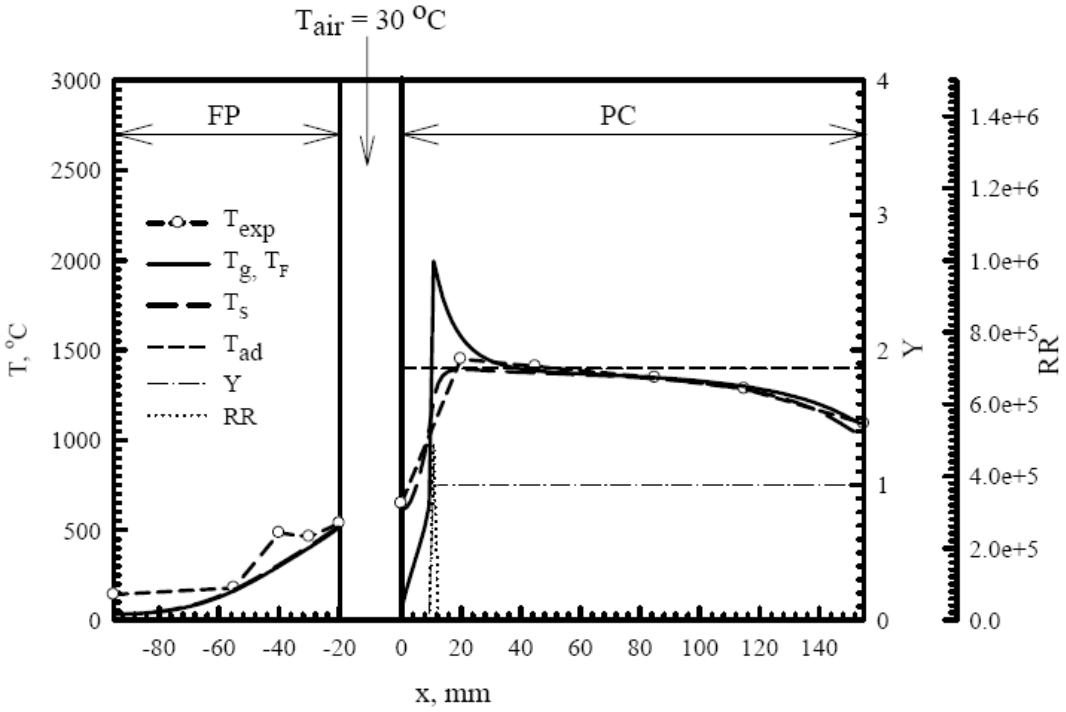

Figure 4.7 Comparison between predicted and measured temperature profiles in case of non-preheated air at 5 kW and Φ = 0.6.

For model validation, a comparison to experimental in case of non-preheated air is performed. The temperature profiles of gas and solid as function of x, inside FP and PC are shown in Fig. 4.7, for firing rate of 5 kW and equivalence ratio of 0.6. Even though the fuel and air supplies of LMPB are separated for safety reasons, the matrix-stabilized flame with peak temperature can occur with the flame temperature higher than a corresponding adiabatic flame temperature, the same phenomenon as that of the normal premixed porous burner. In PC section, at upstream of the reaction, the solid temperature is higher than the gas temperature due to solid conduction and solid-to-solid radiation from the post flame zone to the preheat zone. Immediately at downstream of the flame zone, where the gas temperature exceeds the solid temperature, heat is transfer from the gas to the solid. The maximum temperature of 2027 ^{o}C is greater than adiabatic flame temperature, at which the initial temperature of reactant is ambient temperature. In FP section, the

solid temperature is higher than the gas temperature throughout the region of porous therefore fuel is preheated. The solid temperatures of numerical model are good agreement with a measured temperatures from experiment, except at the upstream of PC, and all location in FP have small different from experimental results. The main reason for this difference is related to the preheating effect of air from hot structure in experimental, before entering mixing chamber. The results imply that the numerical model with assumptions of infinitely fast mixing and one-step global irreversible can be used to predict the non-premixed porous burner.

4.4.2 Local energy balance

Fig. 4.8 show the local energy balance of gas phase at FR = 5 kW and $\Phi = 0.6$. CD, RR, CV, INT, and TOT represent the dimensionless gas phase heat conduction, combustion heat release rate, convection, heat transfer between the phase and local total energy, respectively. In FP, CV mainly balances with INT and the positive INT represent heat transferred from the solid to the gas. In PC, at the reaction zone, RR mainly balances with CV. At the pre-flame and post flame zones CV mainly balance with INT. In addition, at the pre-flame zone, the positive INT represent heat transferred from solid to gas phase for preheated mixture before entering into reaction zone. On the other hand, in the post-flame zone, the INT is negative; mean heat is transferred from the hot product to the solid matrix before flowing out from PC.

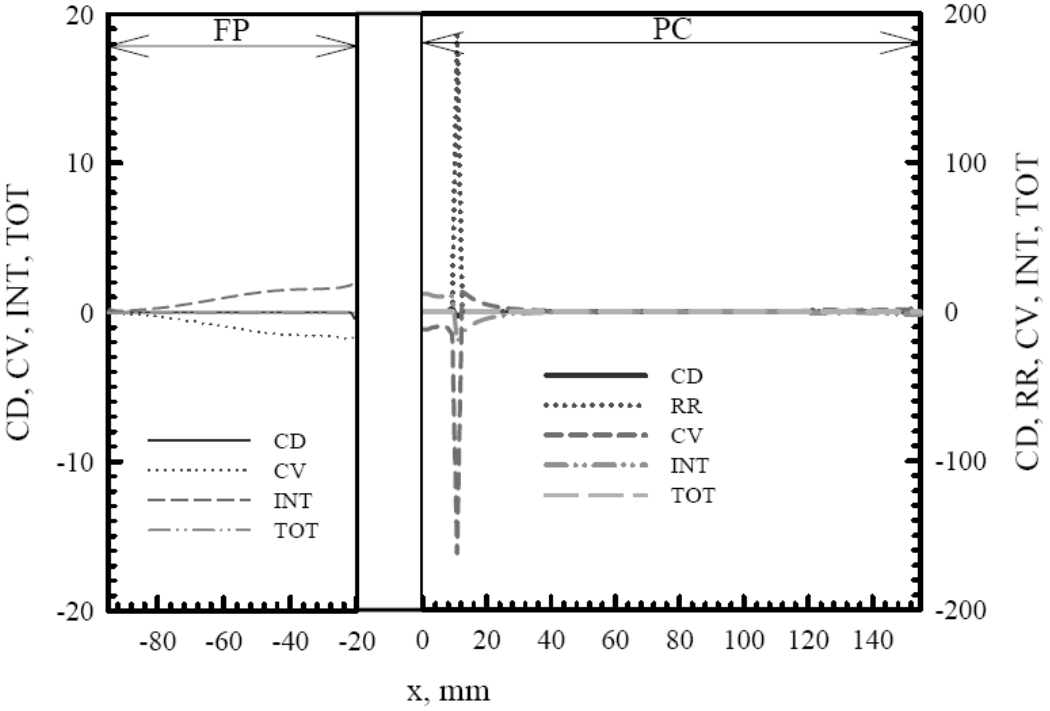

Figure 4.8 Local energy balance gas phase in case of non-preheated air at 5 kW and Φ = 0.6.

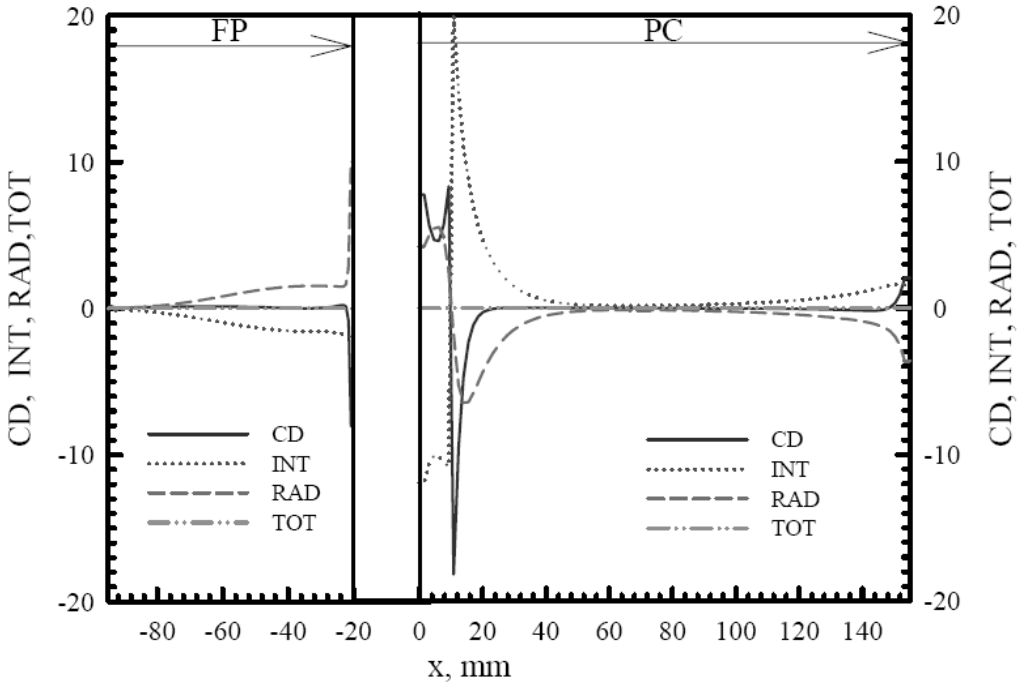

Figure 4.9 Local energy balance solid phase in case of non-preheated air at 5 kW and Φ = 0.6.

Fig. 4.9 show the local energy balance of solid phase at FR = 5 kW and Φ = 0.6. CD, INT, RAD, and TOT are the dimensionless solid phase heat conduction, heat transfer between the phase, solid radiation and local total energy, respectively. Almost all of location in FP, INT mainly balances with RAD. Except at the downstream of FP; the CD is more important, because of high temperature different at the end of FP (see Fig. 4.6). In PC, almost all of location, INT balance with RAD. At around the reaction zone, CD and RAD are mainly balanced with INT; and at downstream of PC, CD and INT are mainly balanced with RAD. Moreover, the sign of INT is opposite to the INT of gas phase. The total energy balance for gas and solid phase (TOT) for all of location both in FP and PC are approached zero. Thus, the global energy balance is 0.2809566 %.

4.4.3 Radiative heat flux and divergence of net radiative heat flux

Fig. 4.10 shows the radiative heat flux in case of non-preheated air at 5 kW and Φ = 0.6. The H^+ and H^- mean radiative heat flux, which direction from left to right, and right to left respectively. The H^n mean net radiative heat flux, which is summation of H^+ and H^-. In PC, at the pre-flame zone heat is radiated from the reaction zone to the upstream end, then heat is radiated from porous PC to FP (negative H^n). In FP, heat is radiated from the hot zone (downstream zone) to the cooler zone (upstream zone), thus the H^n is negative near the end of downstream. While at the post-flame zone of PC, heat is radiated from the reaction zone to the downstream zone (positive H^n).

Fig. 4.11 shows the divergence of net radiative heat flux, DHT at 5 kW and Φ = 0.6. The negative and positive values of DHT mean the porous is absorber and emitter respectively. At the pre-flame zone of PC, the solid matrix absorbs heat from the flame zone. While at the post-flame zone of PC, heat is transferred convectively from the hot gas to the solid matrix. Immediately, the solid matrix emits heat to the upstream and downstream zone of porous PC. In FP for all of location, the solid matrix is absorber.

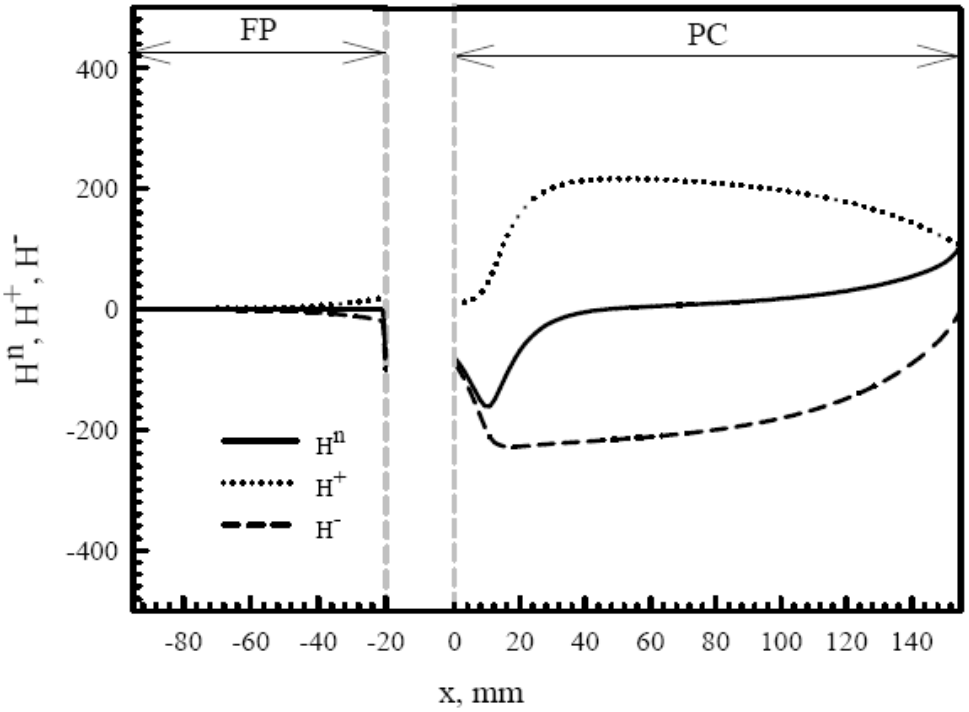

Figure 4.10 Radiative heat flux in case of non-preheated air at 5 kW and Φ = 0.6.

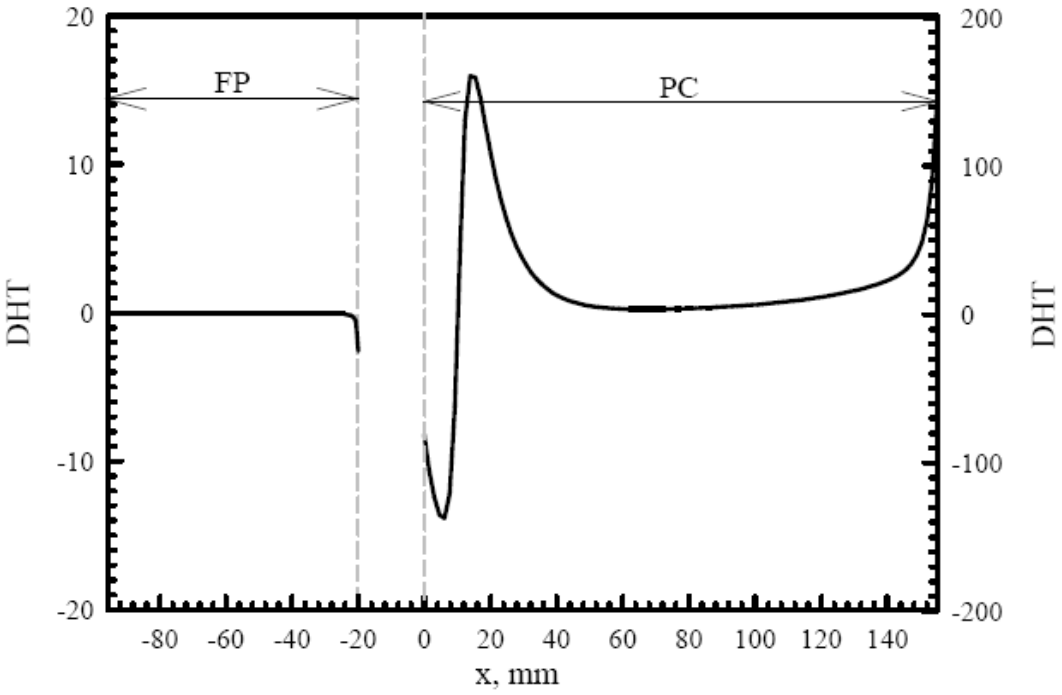

Figure 4.11 Divergence of net radiative heat flux in case of non-preheated air at 5 kW and Φ = 0.6.

4.4.4 Effect of Φ

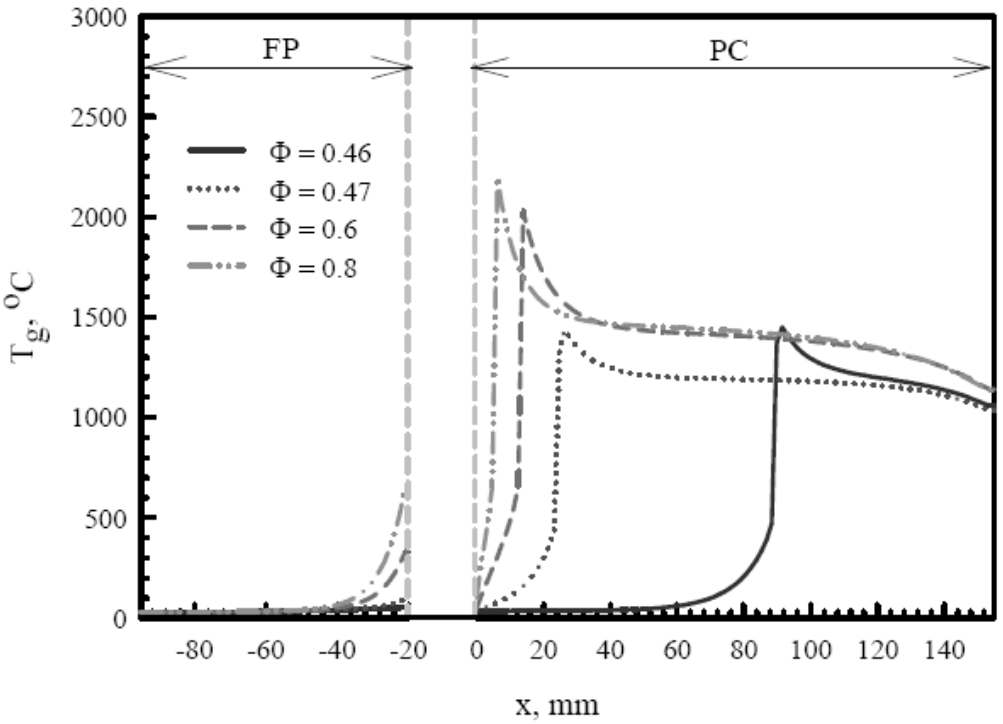

Figure 4.12 Effect of Φ on predicted gas temperature in case of non-preheated air at 5 kW.

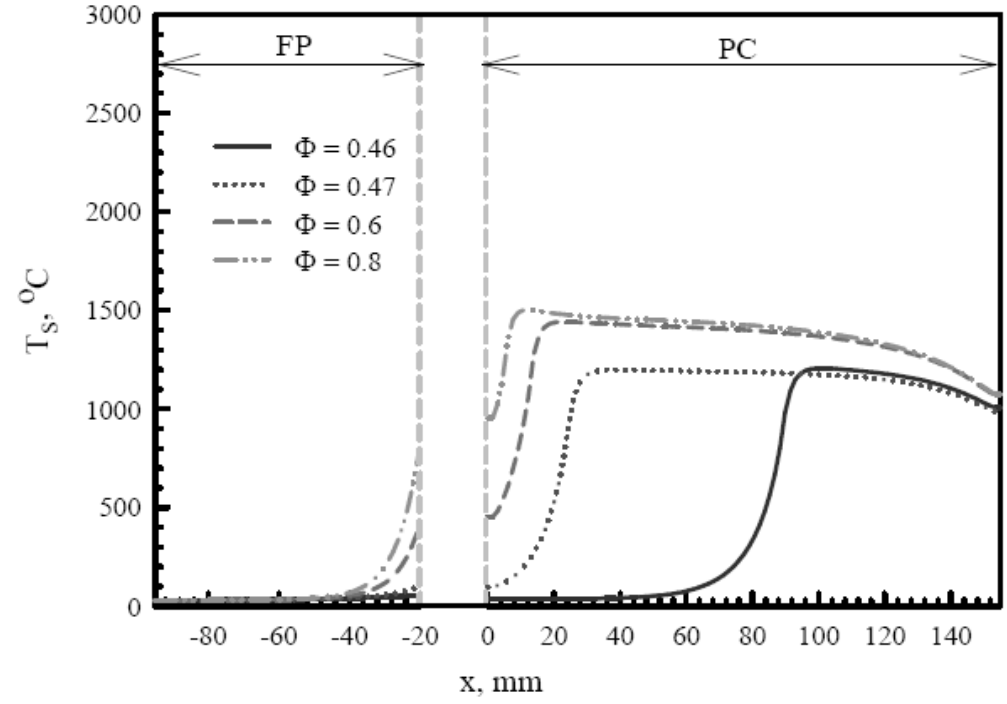

Figure 4.13 Effect of Φ on predicted solid temperature in case of non-preheated air at 5 kW.

Fig.4.12 and 4.13 show the effect of equivalence ratio, Φ for firing rate of 5 kW, on the gas and solid temperatures profiles respectively. The equivalence ratio is an important physical property of a combustible mixture, which indicates the quality of mixture and strongly affects the flame temperature. In this work, Φ is increased by decreasing the air flow rate at a fixed FR. When Φ increase from 0.46 to 0.8, the gas and solid temperature both in FP and PC are increased. Furthermore, the reaction zones move to upstream of PC on account of increasing mixture quality.

4.5 Results and discussion in case of preheated air

4.5.1 Model validation

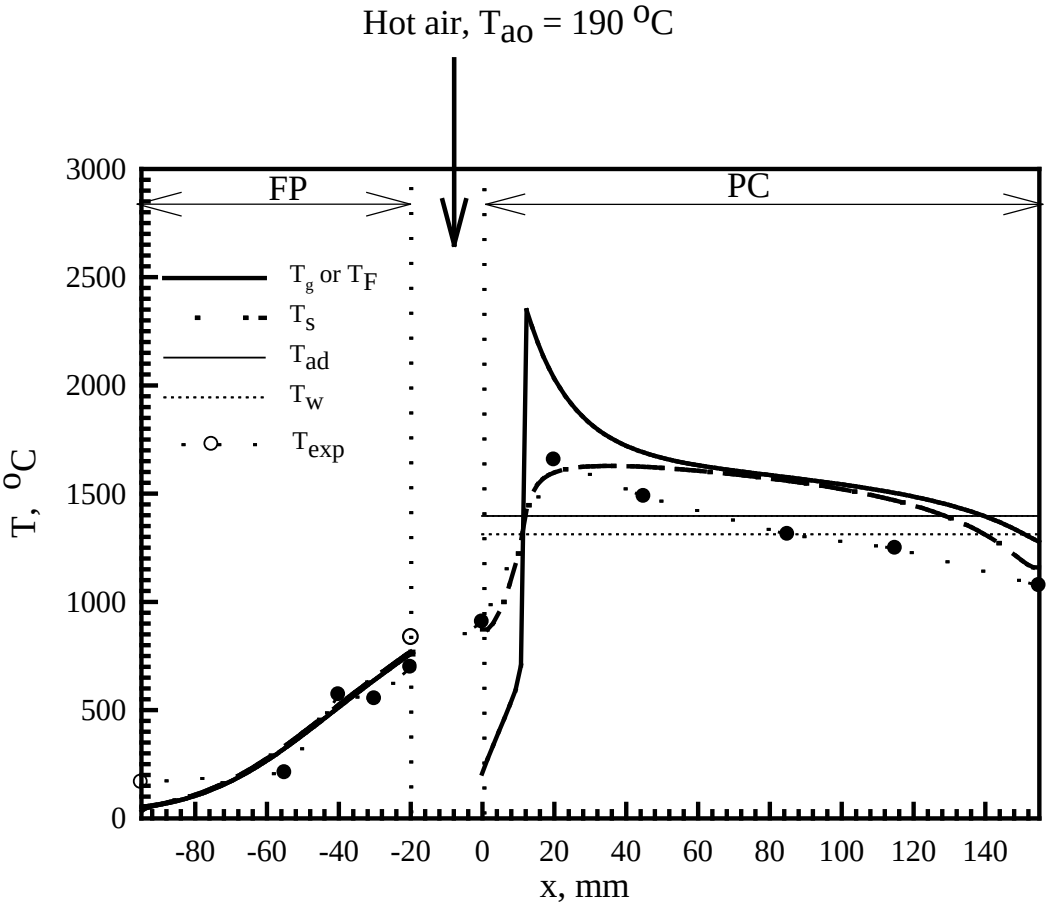

Figure 4.14 Comparison between predicted and measured temperature profiles in case of preheated air at 5 kW and Φ = 0.6.

Figure 4.14 shows typical calculated temperature profiles of gas and solid for firing rate FR = 5 kW and equivalence ratio Φ = 0.6. At the upstream region of the reaction zone in PC $(0 \le x \le 14)$, the solid was hotter than the gas, thus the solid phase enhanced heat transfer to the gas phase. On the contrary, at the post-flame zone in PC $(14 \le x \le 160)$, where the gas temperature was higher than the solid temperature, the gas phase transferred heat to the solid phase. Simultaneously, the solid matrix recirculated heat from the post-flame zone to the pre-flame zone by solid to solid conduction and radiation. Thus, the gas temperature decreased before flowing out from the system. In addition, the maximum gas temperature was higher than the adiabatic flame temperature due to internal heat recirculation. In FP, for all locations, the solid phase temperature was higher than the gas fuel temperature, thus heat was transferred from the hot solid to the gas fuel. This indicated that the fuel was preheated before mixing with the hot air inside the mixing chamber. The numerical results yielded the same trends as those of the experimental ones. At the downstream zone of PC, the predicted solid temperature T_s was higher than the measured ones T_{exp} because heat was lost to the surroundings. The results confirmed that the numerical model with assumptions of infinitely fast mixing and one-step global irreversible reaction can be used to predict the non-premixed porous burner. Wall temperature of 1315 ^{o}C is predicted, yielding preheated air temperature of T_{ao} = 190 ^{o}C before mixing with the fuel followed by combustion in the PC.

4.5.2 Local energy balance

Figure 4.15 and 4.16 show the local energy balance of gas and solid phase at FR = 5 kW and Φ = 0.6, respectively. HLW is dimensionless heat loss from the hot gas in PC to the wall. Energy balance both in FP and CV has the same trends as in case of non-preheated air. Except local energy balance of gas phase in case of preheated air, has an addition term (HLW), which represents preheated air energy. HLW has negative sign all of position that is heat lost from the hot gas in PC to the wall. The local energy is balanced for all of location both in FP and PC (TOT are approached zero). Thus, the global energy balance is 0.2973268 %.

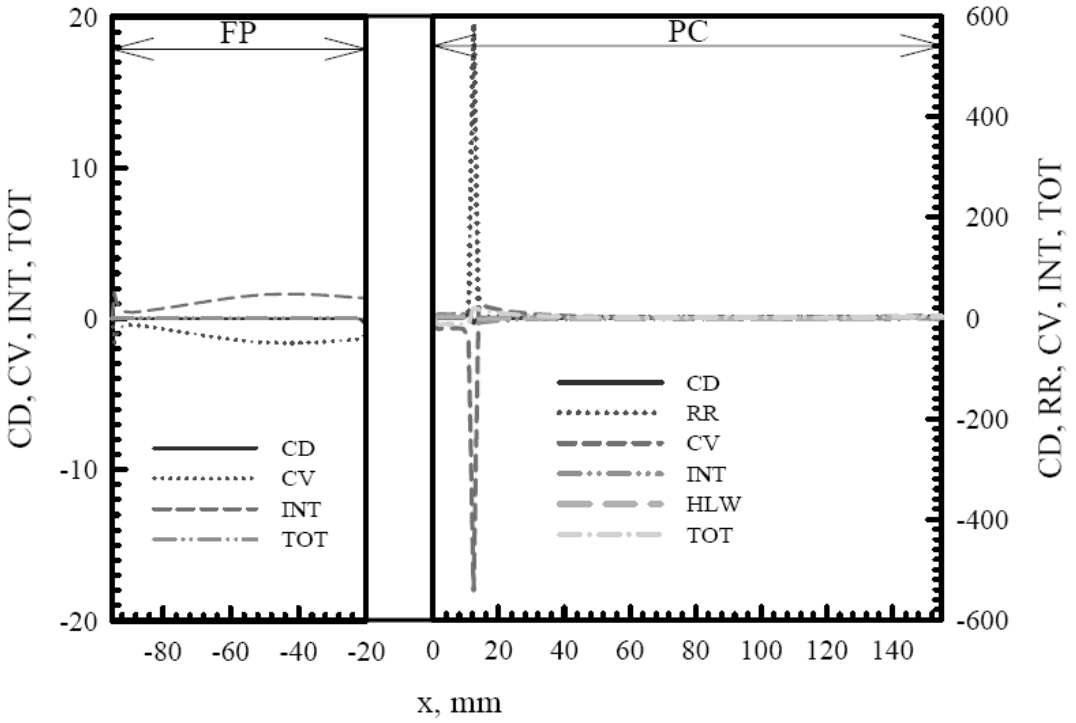

Figure 4.15 Local energy balance gas phase in case of preheated air at 5 kW and Φ = 0.6.

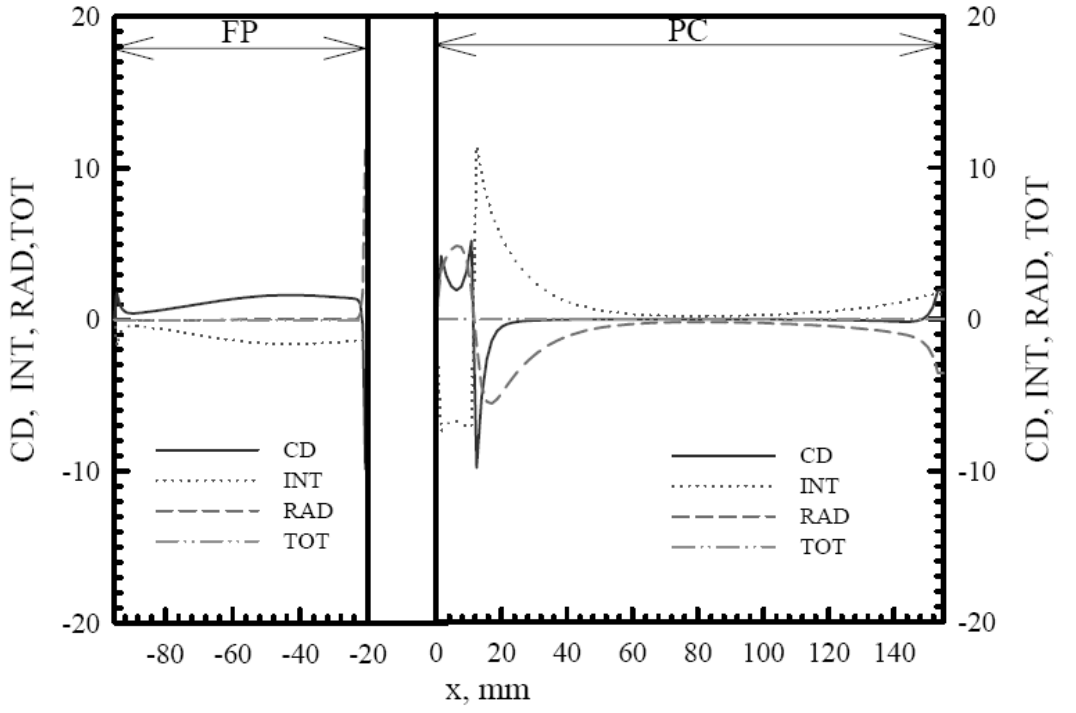

Figure 4.16 Local energy balance solid phase in case of preheated air at 5 kW and Φ = 0.6.

4.5.3 Radiative heat flux and divergence of net radiative heat flux

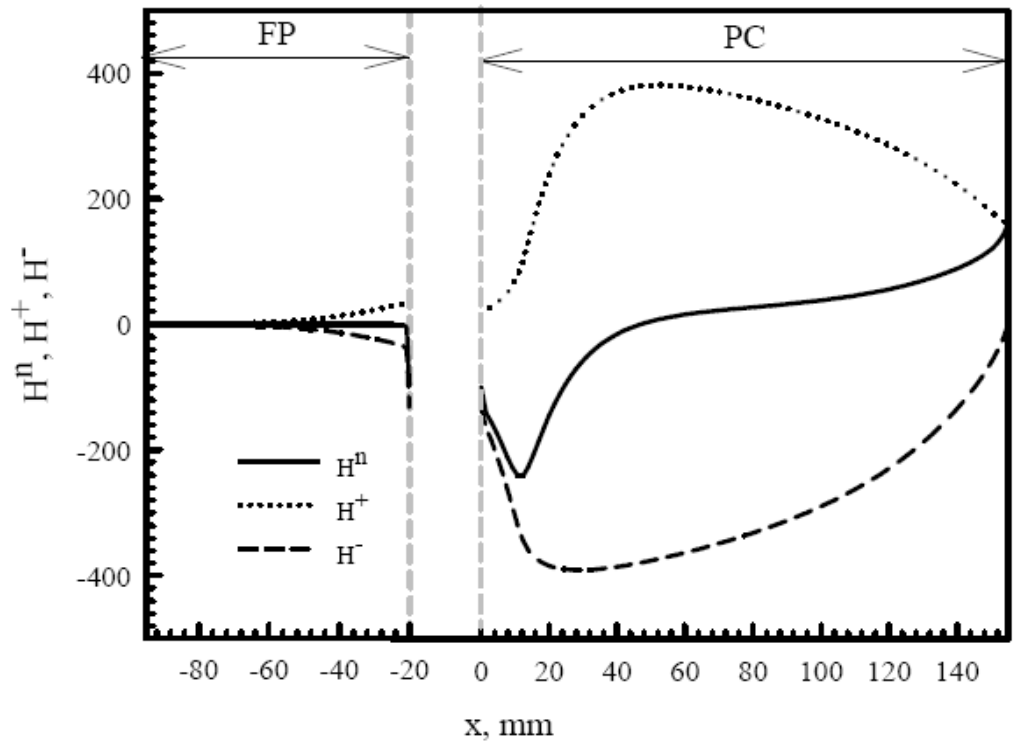

Figure 4.17 Radiative heat flux in case of preheated air at 5 kW and Φ = 0.6.

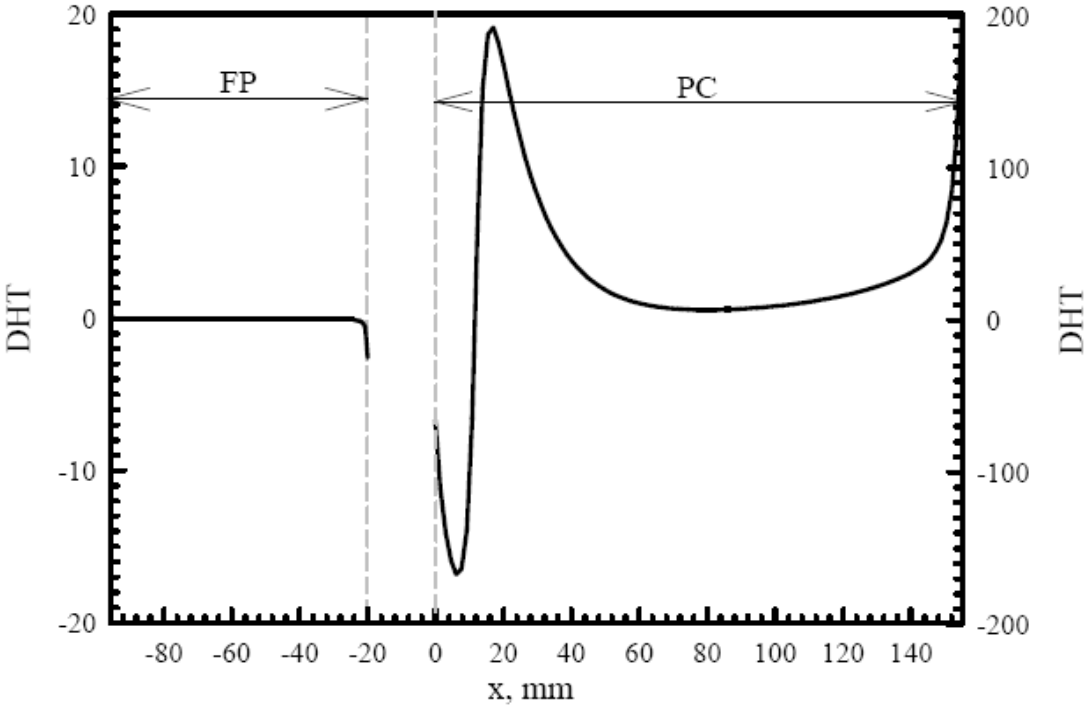

Figure 4.18 Divergence of net radiative heat flux in case of preheated air at 5 kW and Φ = 0.6.

Fig. 4.16 and 4.17 show radiative heat flux and divergence of net radiative heat flux respectively, in case of preheated air at 5 kW and Φ= 0.6. The results show the same trend as in case of non-preheated air, which show in previous section.

4.5.4 Effect of Φ

Fig.4.19 and 4.20 show the effect of Φ in the range of 0.5 – 0.85 for FR of 5 kW on the predicted, T_g and T_s respectively. The graph shows that, increasing Φ leads to a monotonous increase in the temperature both in PC and FP, and the reaction zone is shifted toward the upstream zone of PC. This phenomenon is same as in case of non-preheated air. In addition, operating with preheated air provide higher flame temperature than operating in case of non-preheated air at the same Φ.

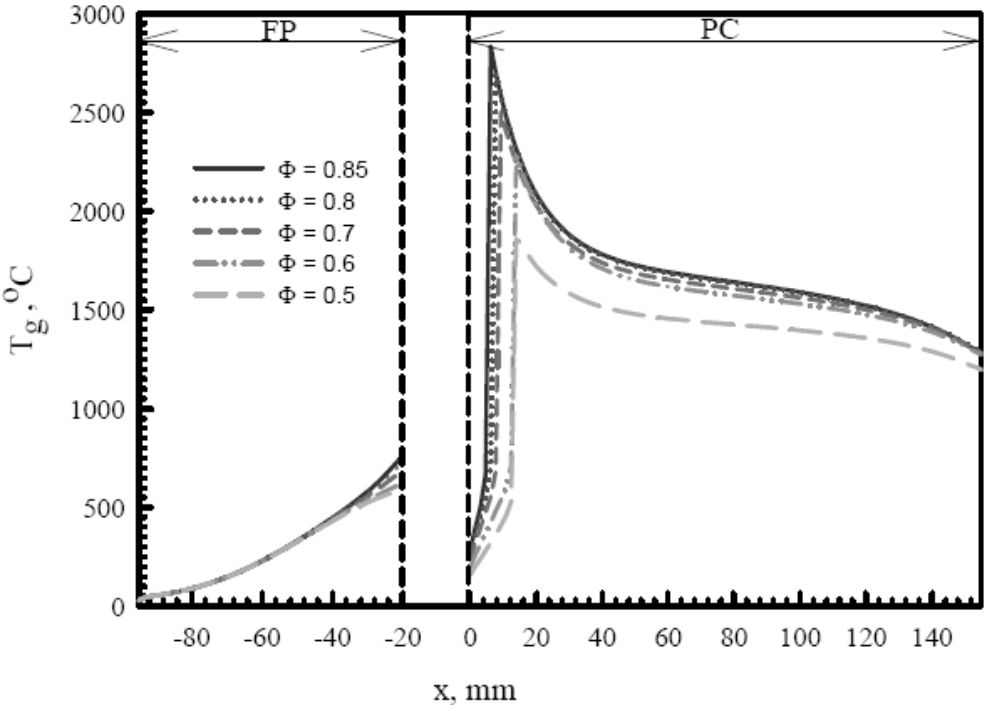

Figure 4.19 Effect of Φ on predicted gas temperature in case of preheated air at 5.74 kW.

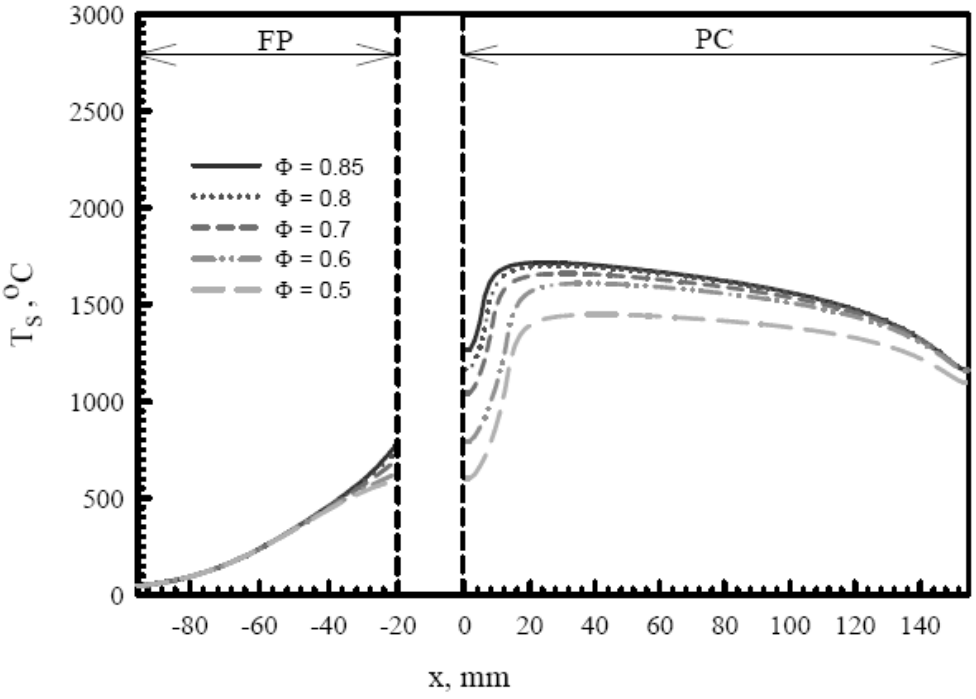

Figure 4.20 Effect of Φ on predicted solid temperature in case of preheated air at 5.74 kW.

4.6 Comparison between non-preheated air, preheated air and SLB

Fig.4.21 shows the heat recirculation efficiency, η_{rec} as a function of Φ of LMPB in case of non-preheated air and SLB at FR = 5 kW. The SLB (Single layer burner) is the premixed LPG/air combustion in porous medium, which has the same physical properties as PC. The η_{rec} are reported for range of equivalence ratio for firing rate of 5 kW. Consideration of LMPB in case of non-preheated air, when increasing equivalence ratio, heat recirculation from FP is increased but heat recirculation from PC is decreased due to moving back of flame zone to upstream. In comparison, heat recirculation efficiency of LMPB is higher than heat recirculation efficiency of SLB for all value of equivalence ratio because LMPB has two preheat zones, while SLB has only one preheat zone.

Fig.4.22 shows the η_{rec} as a function of Φ in case of preheated at FR = 5 kW. The $\eta_{rec,air\ jacket}$ is increased with increasing Φ because of decreasing of air flow rate. The calculated $\eta_{ec,FP}$ and $\eta_{rec,PC}$ is decreased with increasing Φ. The increasing

$\eta_{rec,FP}$ and decreasing $\eta_{rec,PC}$ with increasing Φ is the same trend as non-preheated air case (refer figure 4.21).

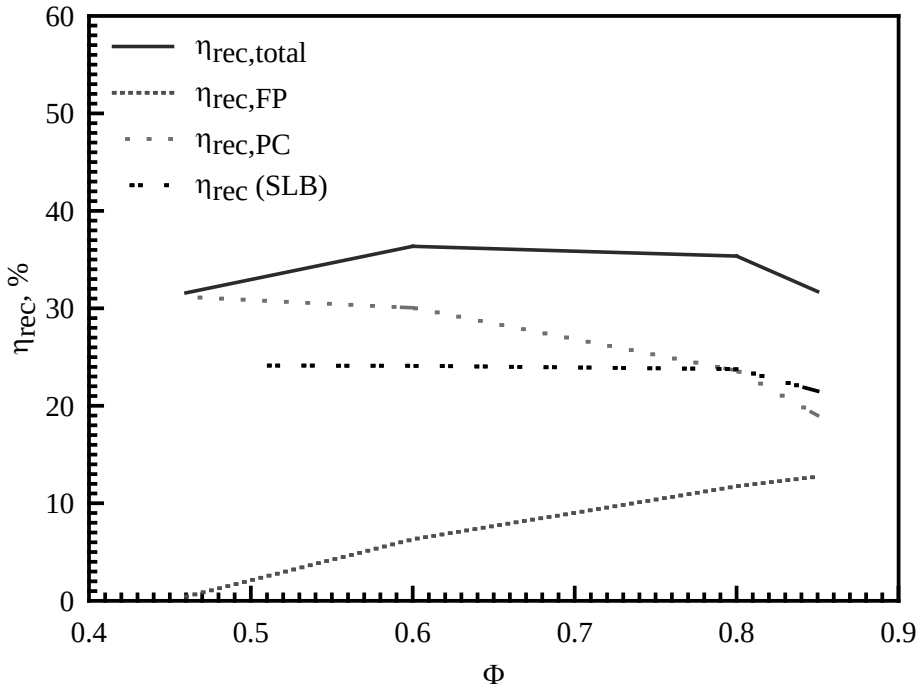

Figure 4.21 η_{rec} as a function of Φ in case of non-preheated air at FR = 5 kW.

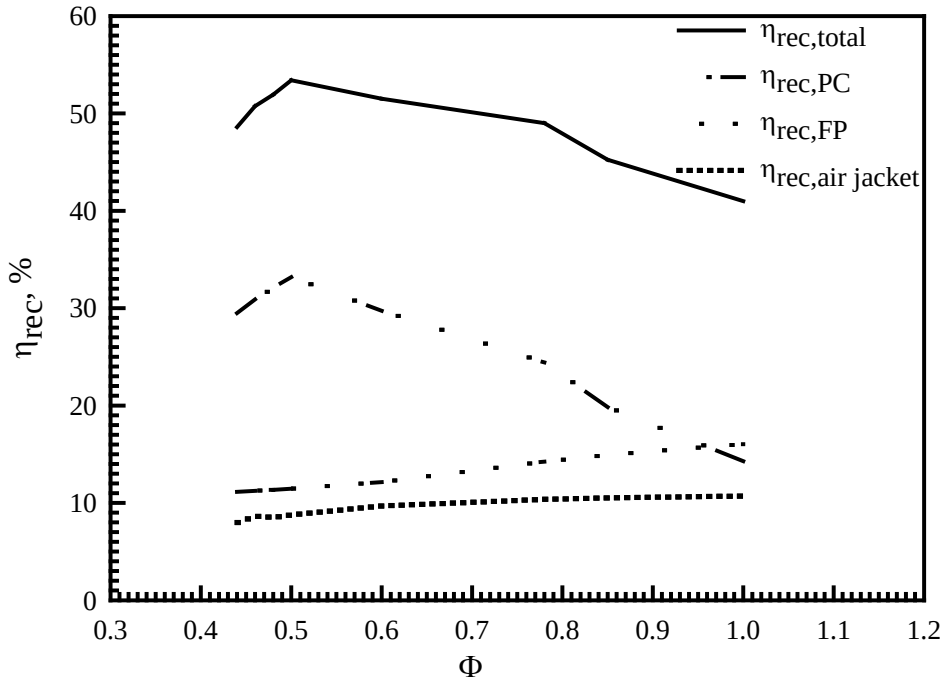

Figure 4.22 η_{rec} as a function of Φ in case of preheated air at FR = 5 kW.

Figure 4.23 shows the η_{rec} as a function of Φ in case of SLB, non-preheated air and preheated air at 5 kW. The graph show that the LMPB both in cans of non-preheated and preheated air are provided higher heat recirculation than normal premixed porous burner, SLB. Beside in case of preheated air provide the highest heat recirculation efficiency for all of Φ, because of having three preheated zones.

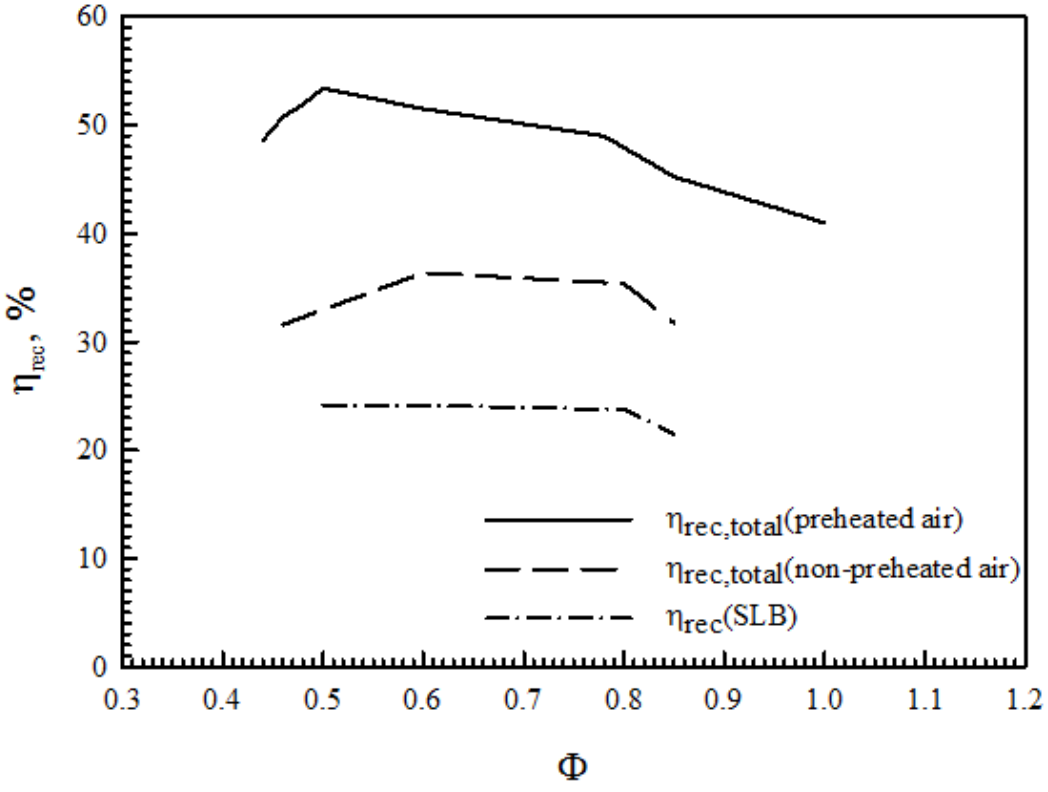

Figure 4.23 η_{rec} as a function of Φ of preheated air, non-preheated air and SLB at FR = 5 kW.

Figure 4.24 shows a comparison of radiant output efficiency η_{rad} between numerical results and experimental ones in case of non-preheated and preheated air of LMPB at FR = 5 kW. The numerical results of the SLB are also shown for comparison. The measured radiant output efficiency for the LMPB is calculated from the corresponding measured temperature. Obviously, The LMPB in case of preheated air obtain highest η_{rad}. The two case of LMPB yields a higher predicted radiant output efficiency than does the SLB throughout the range studied of Φ $(0.42 \le \Phi \le 1.0)$ because of higher heat recirculation efficiency for the LMPB. Consideration in case of preheated air of LMPB, the measured radiant output

efficiency is relatively lower than the predicted ones, because heat is lost to the surroundings during the experiment and this effect was not taken into account in the model. As the equivalence ratio Φ is less than 0.8, the measured radiant output efficiency in case of preheated air almost linearly increased with Φ because of an increase in the combustion temperature in the PC. A further increase in Φ beyond Φ > 0.8 leads to a decrease in the measured radiant output efficiency. This may be attributed to the lowering of the combustion temperature caused by the aforementioned poor mixing followed by an incomplete combustion within the PC.

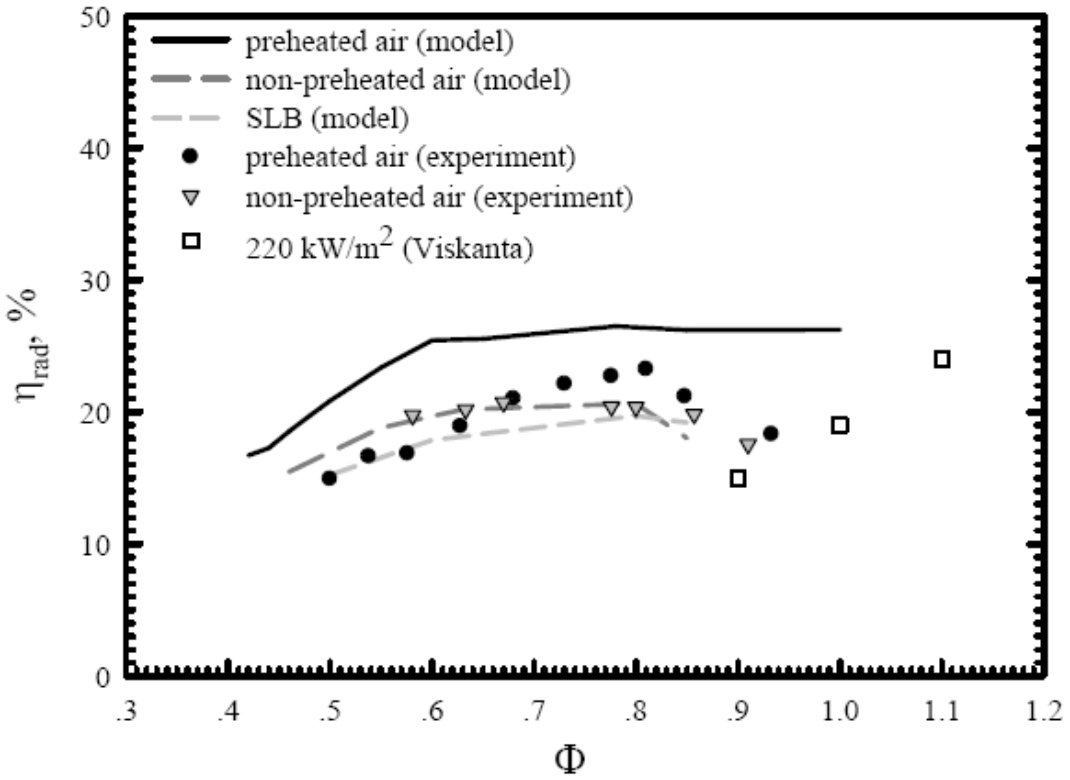

Figure 4.24 η_{rad} as a function of Φ of preheated air, non-preheated air and SLB at FR = 5 kW.

In case of non-preheated air, a numerical result is small difference from experimental, which is not same as preheated air case. Although in experiment has heat lost and the air does not flow through the air jacket for preheating, but the air remain preheated by the hot structure of system before enter mixing chamber. While, in numerical model does not consider preheating effect by the hot structure. This implies that the experiment has more preheating zone than the numerical model. Preheating effect cancel heat loss to surrounding, thus the numerical and

experimental result is not significant different at almost all of equivalence ratio. At near stiochiometric condition, the η_{rad} of experiment are higher than numerical. Because, at near stiochiometric condition is related to the bad mixing in experiment, which results in longer distance of mixing. As observed from the experiment, the flame is located more downstream than that of modeling. Thus provided the higher radiant output efficiency than calculated from the model.

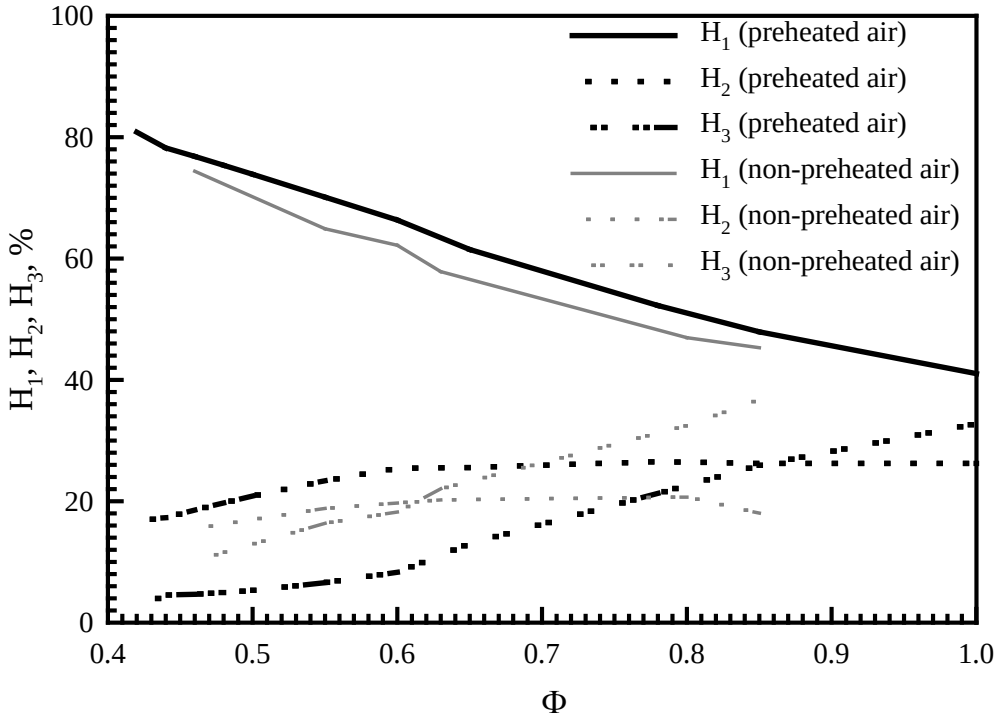

Figure 4.25 Total energy balance as a function of Φ at FR = 5 kW.

Figure 4.25 shows the total energy balance as a function of Φ at FR = 5 kW. H_1, H_2, and H_3 are convection loss at downstream end, emitted radiation toward upstream direction, and emitted radiation toward downstream direction respectively. In the total energy balance in case of preheated and non-preheated air, H_1 is decreased monotonically, while the H_2 is increase at first, and then exhibits quite constant value with increasing Φ. On the other hand H_3 is increased with increasing Φ. Furthermore, the H_3 in case of non-preheated air is higher than in case of preheated air. For this reason, the radiant output efficiency in case of preheated air is greater than in case of preheated air.

4.7 Effect of FR and burner performance

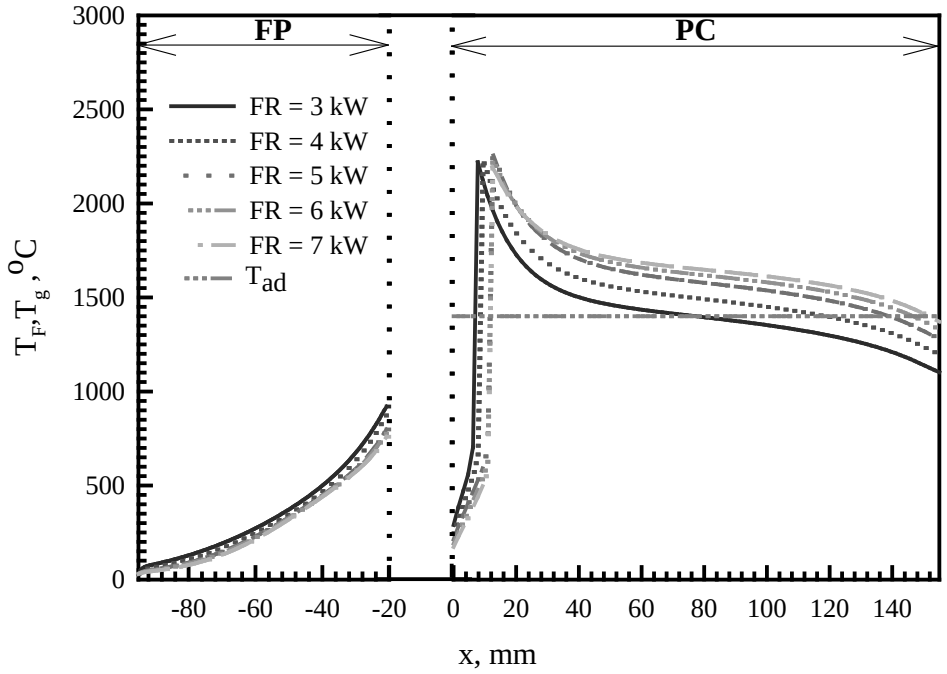

Figure 4.26 Effect of FR on predicted gas temperature in case of preheated air at Φ = 0.6.

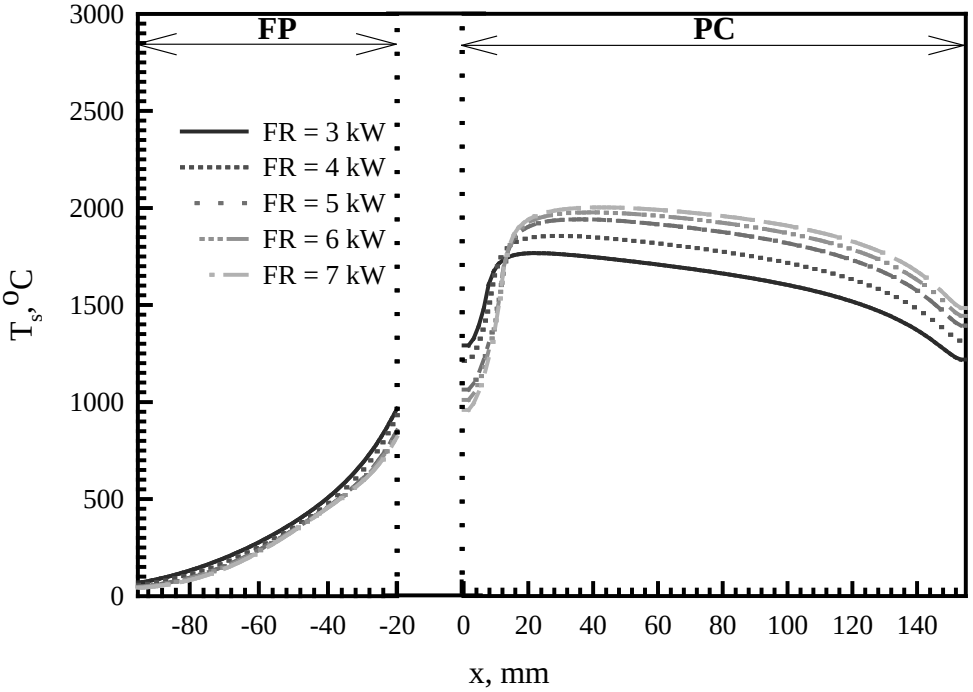

Figure 4.27 Effect of FR on predicted solid temperature in case of preheated air at Φ = 0.6.

Fig. 4.26 and 4.27 show the effect of firing rate, FR on predicted gas and solid temperature in case of preheated air in the range of 3-7 kW at Φ = 0.6. Increasing FR cause to the flame slightly move to the downstream zone of PC. The maximum temperature quite not changes while the temperature at the post-flame zone increases. Because heat radiation to the FP decrease with flame moving to the downstream, and more convective heat transfer from the flame zone to the downstream, when FR increase.

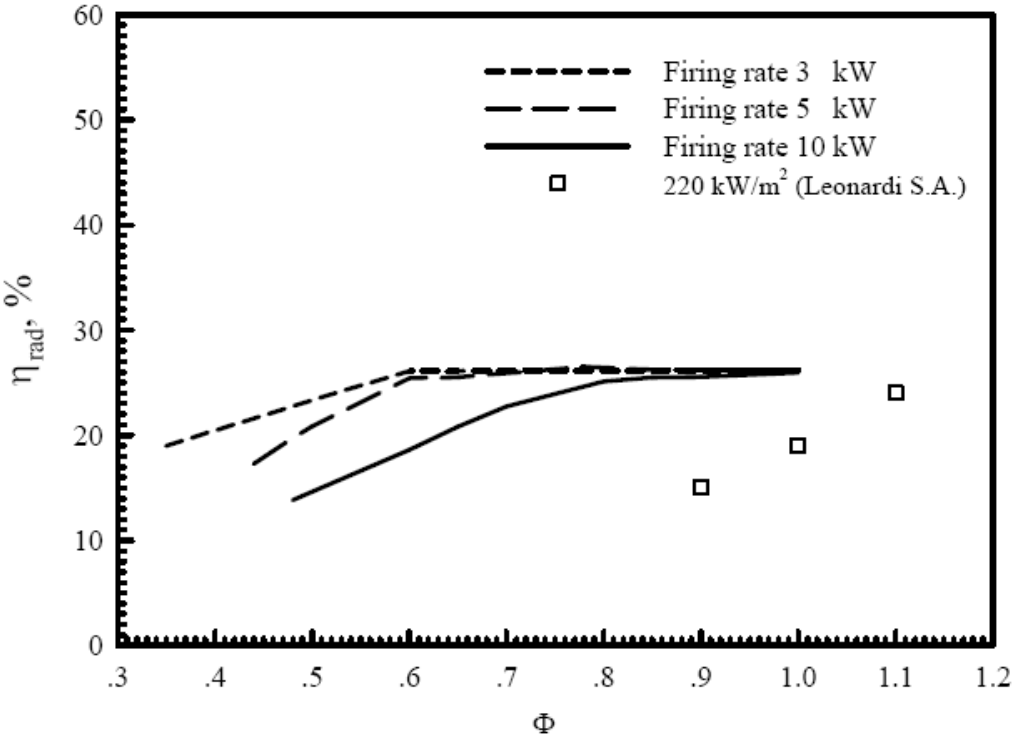

Figure 4.28 η_{rad} as a function of Φ in case of preheated air at FR = 3, 5 and 10 kW.

Fig. 4.28 shows the effect of Φ on the predicted radiant output efficiency η_{rad} at various firing rates FR. At a lean condition (Φ<0.8), η_{rad} largely depends on the FR. Increasing FR at this condition leads to a significant decreasing in η_{rad}. This may be attributed to a large convective loss with a relatively high flow velocity at this condition. Further increasing the FR at this condition further increases the flow velocity, and thus the convection loss. On the other hand, the predicted radiant output efficiency is almost unchanged with FR when Φ is larger than 0.8. This may be attributed to a tradeoff between the increase in the combustion temperature in the PC and the increase in the convective loss when FR is increased. The two

effects cancel each other, and thus the FR does not significantly affect η_{rad}. The LMPB yields higher predicted radiant output efficiency at leaner conditions as compared with those studied by Leonardi et al. (2003).

4.8 Effect of porous combustor type

This section we study influence of porous type using in PC section, on temperature profile and radiant output. By appropriate selection of the porous medium for the combustion section (PC), an optimum flame location and maximum radiant output efficiency may be achieved. From primary study, the results indicated that the maximum radiant output efficiency is provided when the flame located at $x \approx 20$ mm. For the optimum flame location and the maximum radiant output efficiency, the porous material using as PC should have porosity between 0.3-0.5 and the optical thickness in the range of 10-15. Thus in this section only the proper porous material types are studied.

Fig. 4.29 show packed bed of rock is used as PC in this work. The fiber lamellae of Al_2O_3 and SiC foam (refer figure 4.30 and 4.31), which are popularly used in the frame work of combustion within porous media are compared with the porous material is use in this work. The physical properties of porous are summarized in table 4.3.

Fig. 4.32 and Fig 4.33 show effect of porous material using in PC on predicted gas and solid temperature respectively. The graph shows that packed bed of rock, provides highest temperature and the reaction zone locates nearest the middle of PC. Because packed bed of rock has lowest porosity, result in highest interstitial velocity at the same superficial velocity. Therefore, the PC which is packed bed of rock provides highest radiant output efficiency (refer figure 4.34). The result indicates that the packed bed of rock is suitable material type to use as a combustor of non-premixed porous burner.

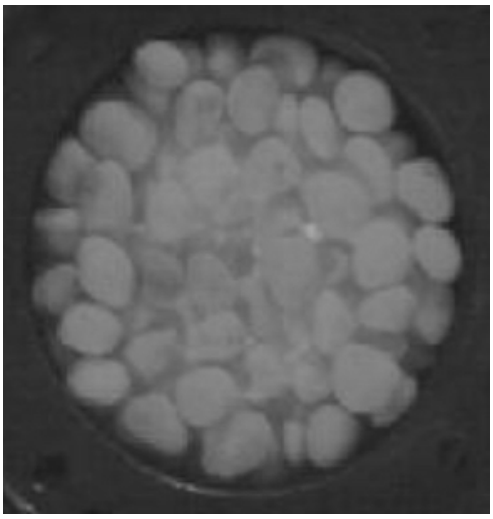

Figure 4.29 Packed bed of rock.

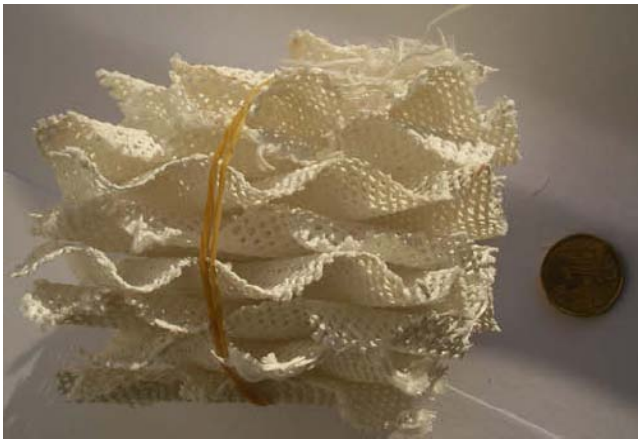

Figure 4.30 Al_2O_3 fiber lamellae.

Figure 4.31 SiC porous foam.

Table 4.3 Physical properties of porous media.

Properties	**Packed bed of rock**	**Al_2O_3 fiber lamellae**	**SiC porous foam**	**Unit**
Porosity, ε	0.361	0.9	0.9	-
Thermal conductivity of pure solid, λ_s	2.3	6.3	46.9	$W.m^{-1}.K$
Effective thermal conductivity of porous, λ_e	1.47	0.63	4.69	$W.m^{-1}.K$
Absorption coefficient, κ	71	70	100	m^{-1}
Optical thickness, τ_e	11.36	11.2	16	$W.m^{-3}.K$
Density of pure solid, ρ_s	2682	3975	3160	kg/m^3
Apparent density, $\rho_s(1-\varepsilon)$	1714	398	316	kg/m^3
Specific heat, c_s	775	765	800	$J.kg^{-1}.K^{-1}$
Porous structure dimenstion, d_p	0.01	0.01	6.00E-04	m
Specific surface area, a_v	380	200	500	m^2/m^3
Volumetric heat transfer coefficient, h_v	4.6×10^4	2.0×10^4	1.1×10^5	$W/m^3.K$

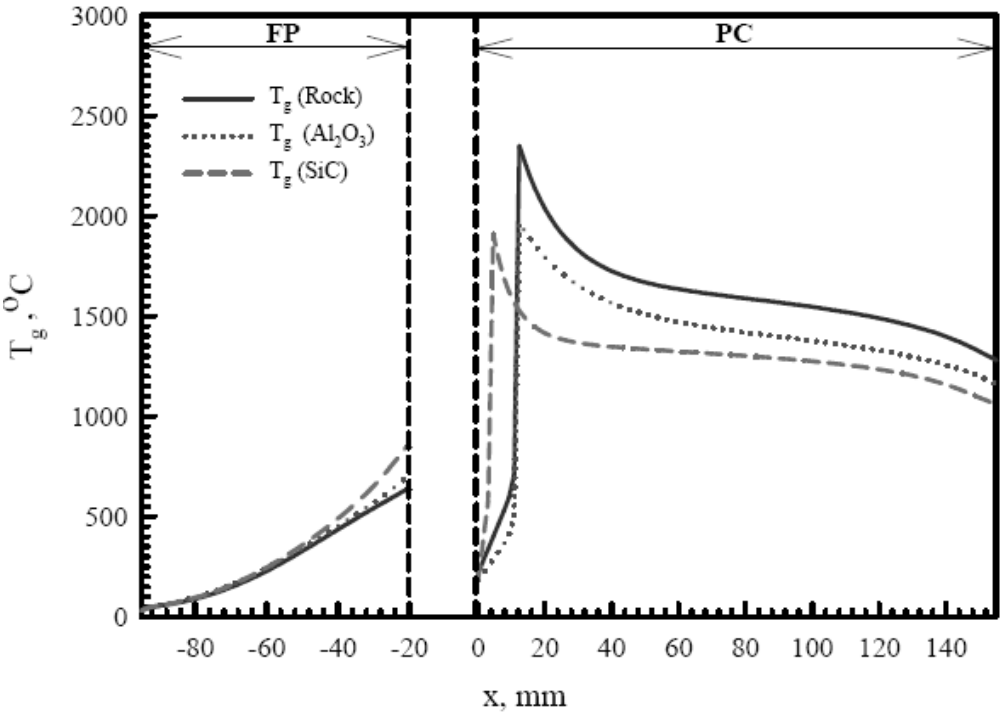

Figure 4.32 Effect of porous material on predicted gas temperature in case of preheated air at 5 kW, Φ = 0.6.

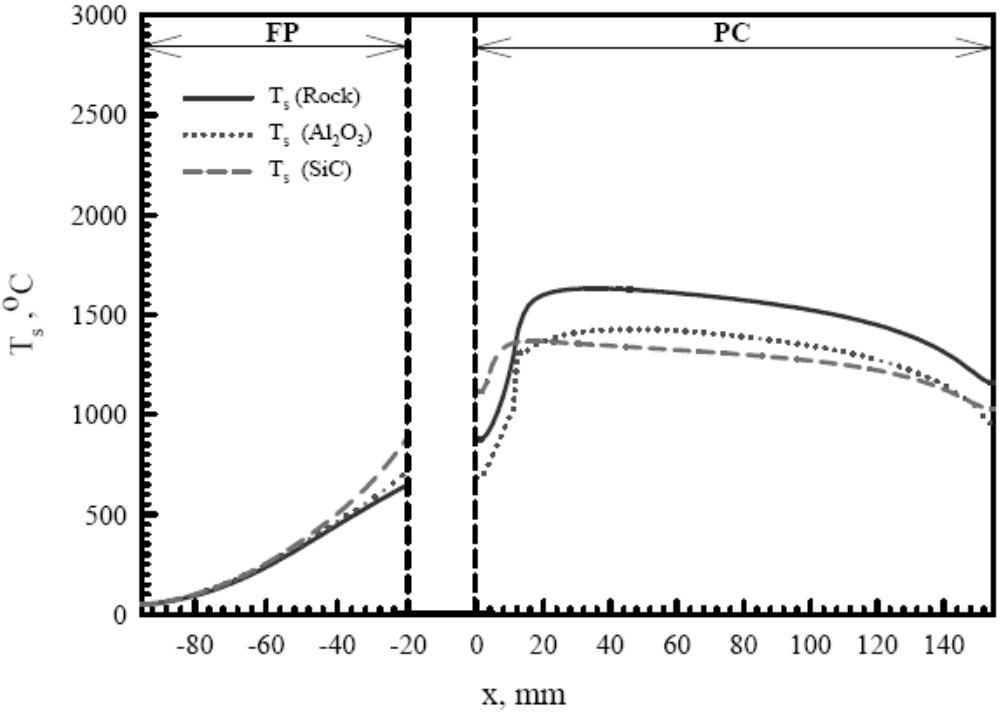

Figure 4.33 Effect of porous material on predicted solid temperature in case of preheated air at 5 kW, Φ = 0.6.

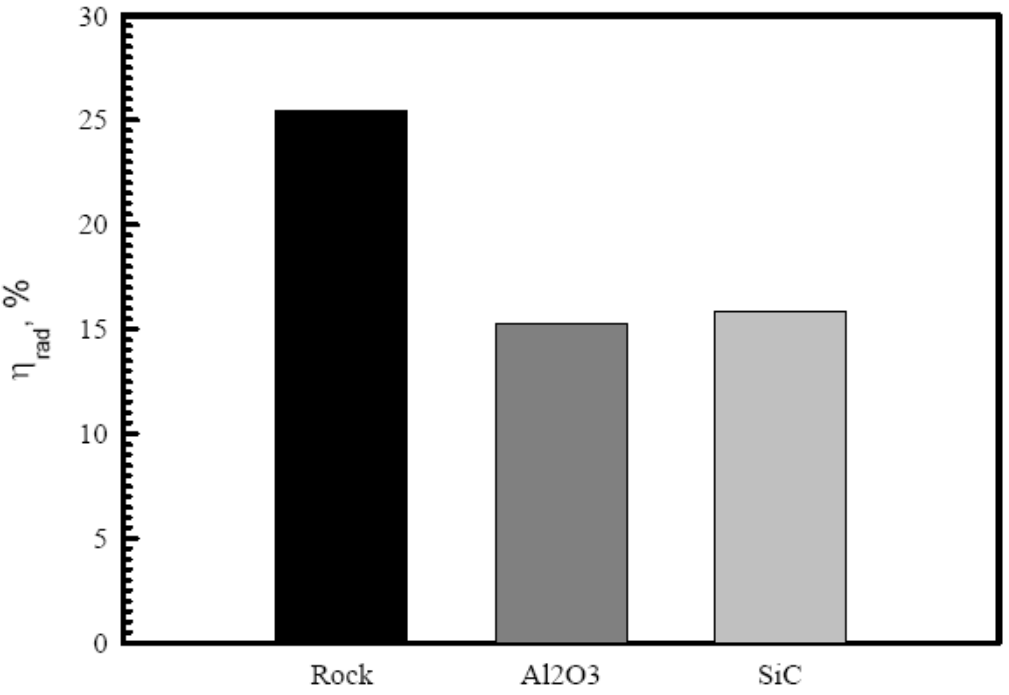

Figure 4.34 Effect of porous material on η_{rad} in case of preheated air at 5 kW, $\Phi = 0.6$.

4.9 Conclusions

An aspect of this chapter is to propose a new concept of a late mixing porous burner (LMPB). A one-dimensional numerical modeling for the LMPB is investigated to study the effects of operating conditions on thermal structures and radiant output efficiency. An infinitely fast mixing process and a single-step global reaction mechanism are considered. The experiment of the LMPB was conducted to validate the model. The conclusions are as follows:

1. The numerical modeling can be used to predict necessary information for burner characteristics and predicts well especially at lean condition ($\Phi<0.8$).

2. The numerical results indicated that the LMPB provides higher radiant output efficiency η_{rad} and higher heat recirculation efficiency η_{recir} than the SLB.

3. LMPB operating in case of preheated air provides higher η_{rad} than in case of non-preheated air.

4. In case of preheated air, equivalence ratio Φ and firing rate FR are important parameters affecting thermal performance of the LMPB. At lean condition (Φ<0.8), the radiant output efficiency η_{rad} is strongly dependent on the equivalence ratio Φ and the firing rate FR. Lowering the equivalence ratio results in lowering the radiant output efficiency. Increasing the firing rate leads to decreasing in the radiant output efficiency. On the other hand, at a relatively high equivalence ratio (Φ>0.8) or near stiochiometric condition, the radiant output efficiency η_{rad} is almost constant irrespective of the equivalence ratio and the firing rate.

5. The porous material using as PC should have porosity between 0.3-0.5 and the optical thickness in the range of 10-15. The PC which is packed bed of rock provides highest radiant output efficiency that indicates that the packed bed of rock is suitable material type to use as a combustor of non-premixed porous burner. Moreover, the packed bed of rock is lowest cost when compare with other two porous type.

6. The LMPB is a good choice for future porous burners because of high η_{rad} and η_{rec}. The LMPB is suggested to be a possible burner for liquid fuels combustion, because of a high heat recirculation efficiency η_{rec} to FP that can be used for evaporation of liquid fuels flowing in the FP.